Aspects of automated seismic interpretation

Aina Juell Bugge

Preface

This work is part of the Industrial PhD-scheme funded by the Norwegian Research Council (NRC), initiated by Lundin Norway AS, the University of Oslo, Department of Geosciences and Kalkulo AS (recently merged with Bluware AS). The supervisors are Dr. Jan Erik Lie, chief geophysicist at Lundin Norway AS, Prof. Jan Inge Faleide from the University of Oslo and Dr. Stuart Clark from the University of New South Wales. From November 2016 – October 2019, author A. Bugge was employed with Kalkulo AS, where Lyuda Vannytska (Kalkulo AS) was the project leader of the NRC project: 268622/O30. Most of this work was conducted at the offices of Lundin Norway AS, the offices of Kalkulo AS and at the University of Oslo, Department of Geosciences. During the course of the PhD, A. Bugge had a 4-month research stay at the University of California, San Diego (2017) and a 1-month research stay at the University of New South Wales, Sydney (2019).

This thesis, entitled "**Aspects of automated seismic interpretation",** was submitted to the Faculty of Mathematics and Natural Sciences at the University of Oslo in accordance with the requirements for the degree of Philosophiae Doctor (Ph.D.), November 2019. The first chapter of the thesis covers the motivation, objectives and scope. The second chapter gives the scientific background relevant for this thesis. The third chapter gives a summary of the results and implications of each of the papers resulting from this work, while chapter four takes on the conclusions and outlook. The articles themselves, two published, one submitted, and one manuscript prepared for submission, are documented in chapter six. To supplement our published journal papers, we have created open-source code repositories at **github.com/ajbugge**.

Acknowledgements

List of Scientific Manuscripts arising from this thesis

Paper I – **Bugge, A. J.**, S. R. Clark, J. E. Lie, and J. I. Faleide, 2018, *A case study on semiautomatic seismic interpretation of unconformities and faults in the southwestern Barents Sea*: Interpretation, **6**, SD29-SD40.

Paper II– **Bugge, A. J.**, J. E. Lie, A. K. Evensen, J. I. Faleide and S. Clark, 2019. *Automatic extraction of dislocated horizons from 3D seismic data using non-local trace matching*: Geophysics, Geophysics, **84**(6), IM77-IM86.

Paper III – **Bugge, A. J.,** J. E. Lie, A. K. Evensen, J. I. Faleide, O. Kolbjørnsen and E. H. Nilsen 2019. *Data-driven identification of stratigraphic units in 3D seismic data using unsupervised machine learning (HDBSCAN)*, [In review]

Paper IV - *Addressing key aspects of automated seismic interpretation* [manuscript prepared for submission]

List of conference proceedings

In addition to the research papers listed in "List of Scientific Manuscripts", conference abstracts based on the Ph.D. work have contributed to the current state of research. In order to limit the extent of this thesis, these abstracts are not included but referred to in this section.

Poster presentation: Aina Juell Bugge, S. Clark, J. E. Lie, J. I. Faleide (2018), *Semi-Automatic Seismic Interpretation Through the Extraction of Unconformities and Faults*, The American Association of Petroleum Geologists AAPG Annual Convention and Exhibition, Salt Lake City, Utah, USA.

Oral presentation: Aina Juell Bugge, Lie, J. E. (2018), *Automated seismic interpretation*, FORCE Hackathon and Applied Machine Learning and Advanced Analytics with Oil and Gas Data, Norwegian Petroleum Directorate (NPD), Stavanger, Norway

Oral presentation: Aina Juell Bugge, J. E. Lie, S. Clark, (2018), *Automatic Facies Classification and Horizon Tracking In 3D Seismic Data*, First EAGE/PESGB Workshop on Machine Learning, London, England.

Oral presentation: Aina Juell Bugge (2019)**,** *A Data-Driven Workflow for 3D Automatic Seismic Interpretation*, DigEx, Gardemoen, Norway.

Oral presentation: Aina Juell Bugge, J. E. Lie, J. I. Faleide, L. Vynnytska, S. Clark (2019), *Automatic Interpretation in Structurally Complex Seismic Volumes*, The American Association of Petroleum Geologists AAPG Annual Convention and Exhibition, San Antonio, Texas, USA.

Oral presentation: Aina Juell Bugge: J. E. Lie, A. K. Evensen, S. Clark (2019), *A New Data-Driven Seismic Interpretation Workflow Using Unsupervised Machine Learning and Non-Local Trace Matching*, 81st EAGE Conference and Exhibition, London, England.

Oral presentation: Aina Juell Bugge: J. E. Lie (2019), *Aspects of automated seismic interpretation using supervised and unsupervised machine learning,* EAGE Subsurface Intelligence Workshop, Manama, Bahrain [Accepted for oral presentation 8-9 December]

Oral presentation: Aina Juell Bugge, J. E. Lie and E. H. Nilsen (2020), *Generative neural networks for seismic processing,* Biennial geophysical seminar, The Norwegian Petroleum Society, Fornebu, Norway [Accepted for oral presentation 9-11 March]

Other scientific contributions

Aina Juell Bugge, Stuart Clark, Jan Erik Lie, Jan Inge Faleide, (2017), *Semi-automatic interpretation of the Earth's interior,* poster presentation delivered at The Geilo Winter School in eScience, Geilo, Norway, January 15-20.

Aina Juell Bugge (2017), *Automated seismic interpretation*, Guest Lecture delivered at University of Oslo, Department of Geosciences, GEO4240 – Seismic interpretation, April 6th.

Aina Juell Bugge (2018), *AI and Digitalization in seismic interpretation,* Talk delivered at Lundins annual exploration seminar, March 6th, Oslo, Norway

Aina Juell Bugge (2018), *Automatic Interpretation of Subsurface Data*, Talk delivered at the Simula Research Seminar, Son, August 30-31

Aina Juell Bugge (2019), *Automated seismic interpretation*, Talk delivered to students in the Minerals and Energy Resources School at the University of New South Wales, Sydney, January 20th.

Aina Juell Bugge (2019), *Automated seismic interpretation*, Talk delivered at the University of Bergen, Norway, Department of Earth Science, March 18th.

Aina Juell Bugge (2019), *AI and Digitalization*, Talk delivered at Lundins annual Exploration Seminar, May 15th.

Code repositories

Open-source code repositories for each of our published journal papers are available through **github.com/ajbugge**. These repositories are published under the MIT-license and free for anyone to use. Repositories for code used in the papers still in review will be published once the papers are accepted. Current repositories are:

(1) FaultIndividualization, matlab code
(2) HorizonTracker, jupyter notebook

Table of contents

Chapter 1. Introduction

1.1 Motivation

Seismic reflection data have been acquired since the late 1920's and have played an important part of oil and gas exploration since the early 1950's. Seismic reflections represent changes in acoustic impedance in the subsurface, and the geologist interprets these reflections to develop maps of geological surfaces and obtain a conceptual understanding of the geological evolution, such as sedimentation history and tectonic events.

Today, the geologist interprets large fully migrated 3D seismic volumes which are created from acquisition and processing of seismic reflection data. The seismic processing is crucial for the seismic image quality which in turn will affect the seismic interpretation. Due to the subjective parameterization and the many possible realizations of the same seismic volume, the seismic processing is also an interpretive process. Thus, seismic processing and seismic interpretation are both iterative operations in a workflow seeking to accumulate subsurface understanding (Figure 1).
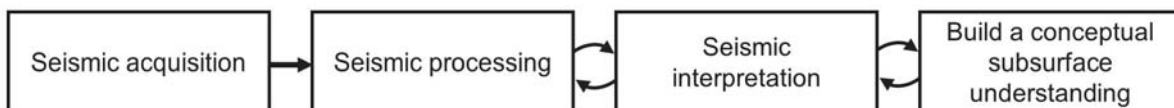
Figure 1. In order to build an understanding of the subsurface from seismic images, seismic reflection data is first acquired and processed to create a seismic image. Then, the seismic images are interpreted. Typically, this is a nonlinear workflow that loops through several iterations of both processing and interpretation.

Ideally, the process of interpreting seismic images is an integrated process based on geophysical knowledge and an intuitive geological understanding. The state-of-the-art seismic interpretation workflow aims to extract qualitative and quantitative information from the seismic data. This typically involves manually placing seed points along targeted geological features, followed by an interpolation between these seed points using coherency-based autotracking tools. Geological features of interest may include seismic horizons, sequence boundaries such as unconformities, and faults. While the interpretation of seismic data is essential in order to accumulate knowledge and build an understanding of the subsurface, some elements of the interpretation workflow, such

as the placing of seed points and the manual quality checking of miscorrelations, can be tedious, subjective and in some cases even trivial.

With increasing computational power, data science continues to evolve and provide new digital tools applicable to various disciplines, including geoscience and thereby seismic interpretation. Most of these tools are based on open-source signal processing, image processing and machine learning algorithms. By utilizing these digital tools to automate the extraction of information from seismic images, we hope to accumulate knowledge and build a subsurface understanding faster and better. However, in order to move towards more data-driven and digitalized seismic interpretation, there is a need to both understand these digital tools, how to adapt them for geophysical data, and how to integrate them with existing geophysical workflows.

1.2 Objective and scope

This thesis investigates aspects of automated seismic interpretation. The overall objective has been to implement digital tools with geological and geophysical knowledge and workflows in order to automatically extract information from seismic data. To reach this objective, we have developed new data-driven methods that take advantage of existing methods and algorithms from the fields of image processing, signal processing and machine learning. In order to address a broad range of key elements of the seismic interpretation workflow, the thesis work has included:

(1) Semi-automatic extraction of individual faults and unconformities from 3D seismic data using image processing tools (Paper I)
(2) Automatic correlation and extraction of seismic multi-horizons from 3D seismic data using non-local pattern recognition for trace matching (Paper II)
(3) Data-driven identification of stratigraphic units in 3D seismic data using unsupervised machine learning (Paper III)
(4) Image to image transformation in order to improve seismic images and to extract attribute information using supervised machine learning (cGAN's) (Paper IV)

Chapter 2. Scientific background

This chapter gives an overview of the scientific background relevant for this thesis. As this thesis covers a scientific field in very rapid development, important papers have been published during the course of this Ph.D study. Some of these papers are included in this chapter, while some of the most recent ones are discussed in the concluding remarks and outlook.

Sub-chapter 2.1, seeks to summarize the evolution of automated seismic interpretation of faults, unconformities, horizons and stratigraphic sequences. The second sub-chapter, 2.2, discusses the use of conditional generative adversarial networks for seismic image to image translation and its implications towards seismic processing and interpretation. Sub-chapter 2.3 summarizes the geological settings on the Loppa High and the Polhem Sub-Platform in the SW Barents Sea, where most of our case examples are taken from.

2.1 Automated seismic interpretation

The last decades, substantial effort has been put into trying to automate the seismic interpretive workflow, e.g. by automatically extracting faults and sequence boundaries or by automatically tracking seismic horizons.

Automatic identification of sequence boundaries and faults was first introduced with the coherence cube in 1995 by Bahorich and Farmer (Figure 2). The coherence cube is generated with a coherence algorithm that obtain similarity measurements of neighboring seismic traces in order to identify and quantify both stratigraphic and structural discontinuities in seismic data. Today, the most commonly used coherence algorithms include cross-correlation (Bahorich and Farmer, 1995), eigenstructure (Gerztenkorn and Marfurt, 1999; Chopra, 2002), and semblance (Marfurt et al., 1998; Hale, 2013). Other geometric attributes, such as curvature (Roberts, 2001) and flexure (Di and Gao, 2016) have also been suggested as alternatives to the coherence cube.
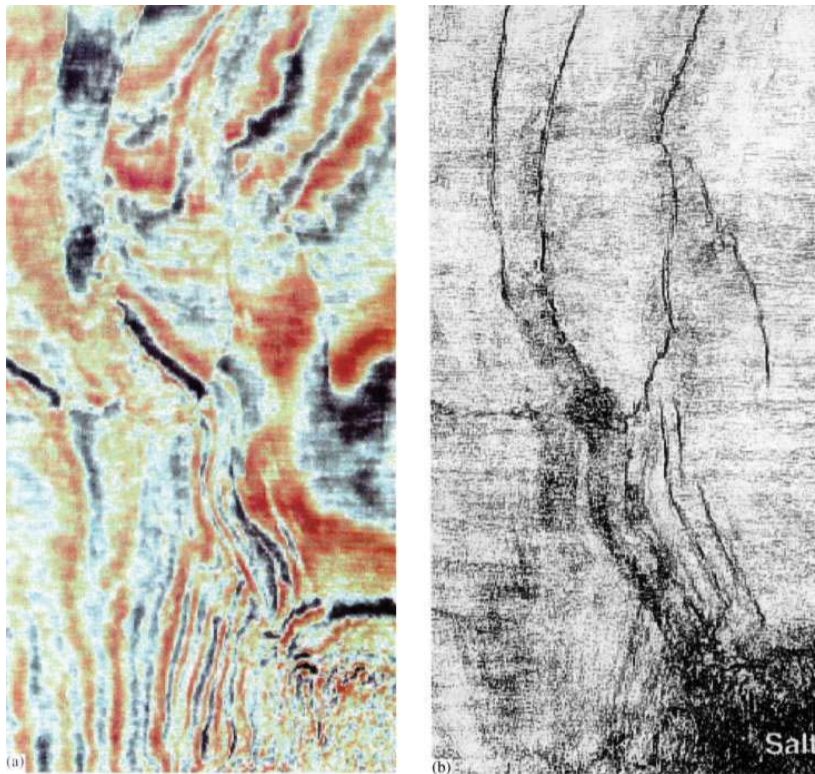
Figure 2. The figure shows a seismic time slice (left) and the same time slice from the coherence cube of the same dataset (right). The coherency cube reveals faults and discontinuities in seismic volumes without the need for manual seismic interpretation (Bahorich and Farmer, 1995).

Autotracking tools for seismic horizon interpretation have been readily available since the mid 1990's and a range of different methods exist. Some of the more interesting ones are based on local reflection slopes (e.g. Bakker, 2002; Lomask et al., 2006), unwrapped instantaneous phase (e.g. Stark, 2003; 2005; Wu and Zhong, 2012) and dynamic time warping (Wu and Hale, 2016a; Wu and Fomel, 2018). However, even with autotracking tools, seismic interpretation relies on some manual effort by an experienced seismic interpreter, such as picking seed points along target horizons or a prior interpretation of unconformities or faults, in addition to manual quality checking of miscorrelated seismic reflections.

Lately, methods using machine learning have been proposed to aid seismic interpretation by highlighting and extracting important information automatically or semi-automatically from the seismic reflection data. Machine learning, often subdivided into supervised and unsupervised, is a subset of artificial intelligence that allows computers to learn from experience and make new predictions on multidimensional data (Figure 3). Supervised machine learning algorithms have

typically been used in interpretive workflows in order to target specific seismic features. Some recent publications on supervised seismic interpretation uses convolutional neural networks (CNN) in order to automate the interpretation of faults (Huang et al., 2017), salt bodies (Waldeland et al., 2018; Di et al., 2018) and seismic facies (Zhao, 2018). With these supervised machine learning workflows, good training data are required, and good training data rely on interpretive experience and prior geological knowledge. Unsupervised learning differs from supervised learning, most importantly because it does not require manually labelled training data. Instead, unsupervised machine learning algorithms find patterns in unlabeled datasets. A typical approach using unsupervised machine learning for automated seismic interpretation is to cluster one or several appropriate seismic attributes. Interesting publications on unsupervised interpretation include automated facies recognition (de Matos et al., 2007; Zhao et al., 2015; Qi et al., 2016), and interpretation of direct hydrocarbon indicators and thin beds causing tuning (Roden et al., 2015; 2017). With unsupervised machine learning, no labels are required, but the approach is sensitive to the structure of the input data and therefore, the selection of different seismic attributes is the limiting factor.
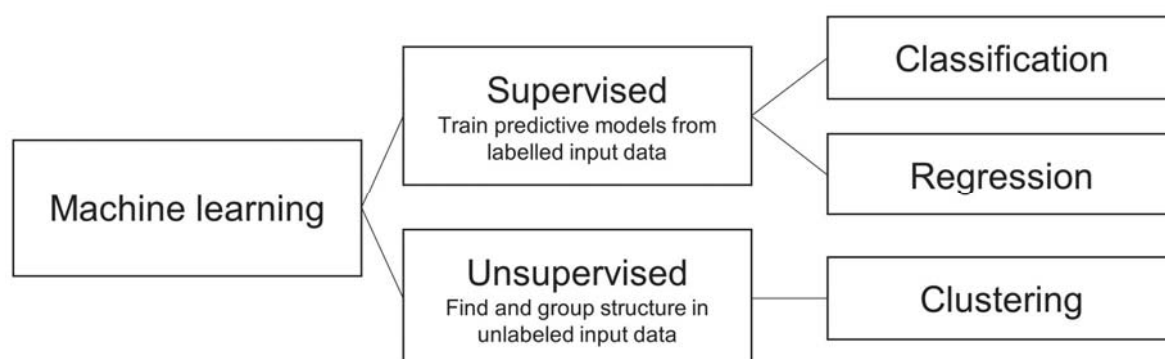
Figure 3: The two main subdivisions of machine learning are supervised and unsupervised learning. Supervised machine learning is usually used for regression or classification, and requires labelled input data, while unsupervised machine learning is used for clustering of unlabeled data.

2.1.1 Unconformities

Unconformities are stratigraphic sequence boundaries that represent changes in a depositional environment due to an erosional event or a non-depositional hiatus. Erosional events are often related to uplift, and erosional boundaries are particularly important to interpret in order to

understand the tectonic movements and the subsequent fill of sedimentary basin. As unconformities represent geological time gaps in seismic images, they can be complicated to identify and interpret both manually and with automatic tools.

Since the introduction of the coherence cube (Bahorich and Farmer, 1995), methods proposed for automated detection of sequence boundaries have typically been based on the principles of traditional seismic sequence stratigraphy (e.g. Barnes et al., 2000; Hoek et al., 2010; Qayyum et al., 2017, 2018). Both Barnes (2000) and Hoek et al. (2010) characterized seismic reflection patterns to generate attributes that highlight angular unconformities and Qayyum et al. (2017, 2018) discussed how one can use semi-automatic Wheeler diagrams (Wheeler, 1958) to detect unconformities. A recent method on automatic unconformity detection, proposed by Wu and Hale (2015a) highlights both angular and parallel unconformities from the calculated difference of two seismic normal structure fields and two structure-tensor fields.

2.1.2 Faults

Faults are discontinuities in the Earth caused by fracturing and displacement of rock volumes. A variety of existing computational and computer-assisted fault interpretation methods are based on the identification of fault attributes such as the coherence cube (Figure 2) (Bahorich and Farmer, 1995) or fault likelihood (Figure 4) (Hale, 2013). One example is "Ant tracking", proposed by Pedersen et al. (2002, 2003) where virtual ants track discontinuities within a coherence cube. Torabi et al. (2016) proposed a way of extracting and digitizing manually selected fault segment coordinates from filtered fault likelihood time slices. Wu and Hale (2016b) defined fault samples based on measured fault likelihood, dip and strike for each pixel in an input image and then used these fault samples to construct fault surfaces with a 3D sampling grid.

Besides attribute-based fault identification, supervised machine learning has shown to be a promising tool for automated fault interpretation Huang et al. (2017) proposed the use of convolutional neural networks trained to learn fault characteristics and predict faults from extracted features in a fault likelihood cube. Some more recent contributions to fault detection using machine learning are included in Chapter 4; Concluding remarks and outlook.
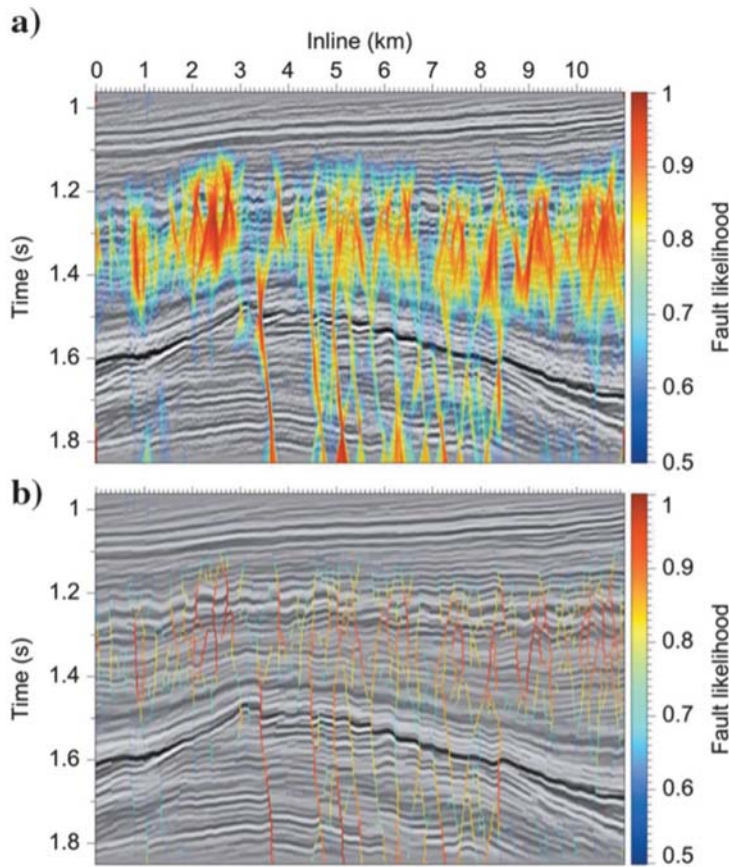
Figure 4. Fault likelihood computed from fault dips θ, (a) before and (b) after thinning (Hale, 2013b)

2.1.3 Seismic horizons

Extracting key horizons and surfaces from seismic images is an important element of the seismic interpretation workflow. The state-of-the art seismic horizon interpretation involves manually selecting seed points along target horizons. However, a range of automated horizon extraction methods has been introduced as alternatives to the process of manually picking seed points (Bakker, 2002; Lomask et al., 2006; Stark, 2003, 2005; Wu and Zhong, 2012; Wu and Hale 2015b, 2016a; Wu and Janson, 2017; Wu and Fomel, 2018). Generally, seismic horizons that are truncated by unconformities or dislocated by faults present difficulties for both manual and automated horizon interpretation.

Bakker (2002) and Lomask et al. (2006) proposed to estimate local reflection slopes using structure tensors and then iteratively fit horizon slopes with the local reflection slopes. These local reflection slopes methods typically track coherent seismic horizons successfully but are sensitive to faults

and other discontinuities. Additionally, local reflection slope methods often cause a tracked horizon to jump from peak to trough or vice versa, due to the lack of amplitude or phase information (Bakker, 2002). Instantaneous phase is commonly used to complement seismic amplitude information for seismic interpretation (Taner et al., 1979). In 2003, Stark introduced a method using unwrapped instantaneous phase to generate relative geologic time (RGT) cubes, and then extracted seismic horizons directly from these RGT cubes. Stark's method was based on the assumptions that coherent seismic horizons follow constant instantaneous phase values and that the unwrapped phase represents relative geologic time in a given seismic volume or image (Stark, 2003, 2005). Wu and Zhong (2012) proposed an extension to Stark's method by implementing horizon and unconformity constraints into a 3D unwrapping process. They showed that the implementation of these constraints significantly improves the reliability of the RGT volume, assuming that the user has unconformities and reliable horizons or segments of reliable horizons prior to the unwrapping operation.

Wu and Hale (2016a) introduced a full interpretive workflow to automatically extract horizons from flattened seismic images (Figure 5). Their workflow included (1) fault identification and unfaulting of seismic images, (2) unconformity identification, (3) unconformity-constrained image flattening and (4) horizon extraction from the flattened seismic image (Wu and Hale, 2015a; 2015b; 2016b). Wu and Hale's (2016a) interpretive workflow addresses many important challenges in seismic interpretation. However, some of the steps related to their fault processing and unconformity processing are complex, which may affect the quality of the flattening operation and in turn, the horizon extraction.
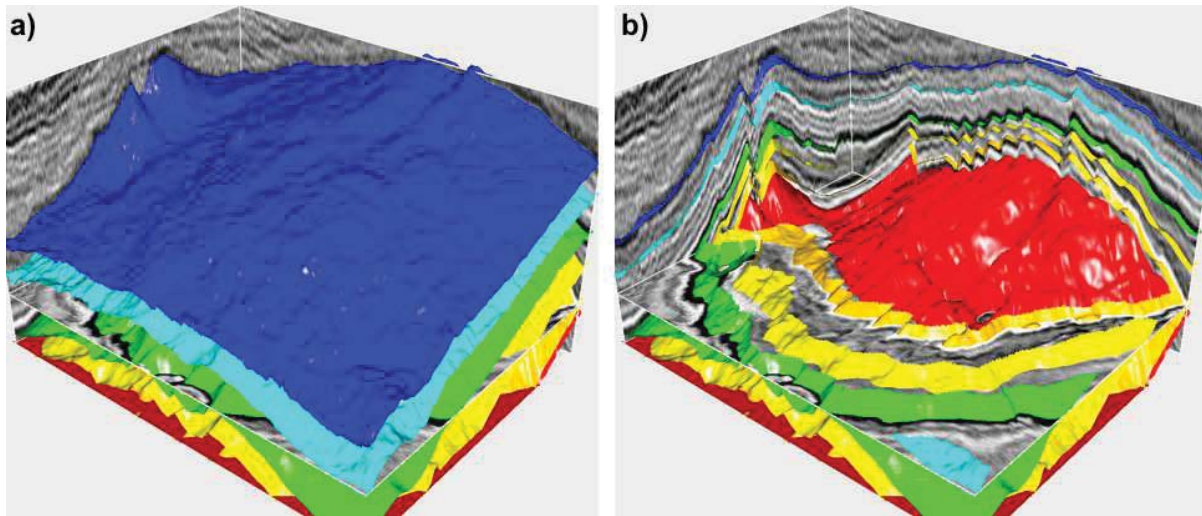
Figure 5. Two 3D sections of automatically extracted seismic horizons from Wu and Hale (2016).

In 2018, Wu and Fomel proposed to extract horizons by fitting, in least-squares sense, the local slopes and multi-grid correlations of seismic traces. Here, the local slopes are used to fit smooth and coherent horizons without structural discontinuities. They calculate the multi-grid correlation using dynamic time warping (Sakoe and Shiba, 1978), and implement this in order to follow consistent phases (e.g., zeros, peaks or troughs) and to track horizons that follow dislocations across faults.

2.1.4 Stratigraphic units

In a typical seismic image, stratigraphic sequences are distinguishable by the different properties of the seismic reflections such as continuity, amplitude and frequency spacing (Badley, 1975). These sequences are units of relatively conformable seismic reflections, i.e. time intervals of similar sedimentation conditions governed by sediment supply and relative sea level, where the top and base sequence boundaries are defined as unconformities or correlative conformities caused by change in sediment deposition or non-deposition (Mitchum et al., 1977). Stratigraphic units can be further divided into packages representing the depositional strata, such as lowstand, highstand and transgressive system tracts. Hence, stratigraphic units and their boundaries that define a fixed geological time are key features in understanding the evolution of sedimentary basins (Vail et al., 1977).

Automated identification of stratigraphic units often involves some sort of texture attribute, either alone, to indicate stratigraphic changes, or in combination with unsupervised machine learning. A typical approach using unsupervised machine learning is to cluster one or several appropriate seismic attributes (de Matos et al., 2007; Zhao et al., 2015; Qi et al., 2016). Additionally, supervised machine learning has been suggested to identify stratigraphy, such as a method by Zhao et al. (2018) that uses a convolutional neural network (CNN) to interpret different seismic facies.

2.2 Seismic image to image translation

In 2017, Isola et al. introduced the use of a conditional generative adversarial network (cGAN) to perform image to image translation to change the style of an image (such as to colorize grayscale images) or to transform real photographs to artistic images. Generative adversarial network (GAN's) was proposed by Goodfellow et al. (2014) and consists of two trained models, a generator and a discriminator. The generator is trained to produce output data, while the discriminator is trained to evaluate if the output data produced by the generator is "real" reference data or "fake" generated data. As for all neural networks, GAN's have a loss function that measures the inconsistency between predicted and actual data, and that optimizes the network parameters. Whereas this loss function must be carefully decided when working with more traditional convolutional neural networks, it is automatically computed for GAN's. Therefore, GAN's are more generic and can be used to solve a range of image classification problems. Whereas as GAN's learn a mapping from random noise vector z to output data y, G: z $\rightarrow$ y, conditional GAN's (cGAN's) condition the generator and/or the discriminator using additional information. This way the cGAN's learn a conditional generative model to map from an observed data x and random noise vector z, to an output data y, G: {x, z} $\rightarrow$ y.

In the image-to-image translation by Isola et al. (2017), their architectural choice for the generator is a U-Net-based network, while the discriminator is a convolutional "PatchGAN" classifier. The U-net architecture, proposed by Ronneberger et al. (2015), is illustrated with Figure 6. This network has 23 convolutional layers and consists of a contracting path (left side) and an expansive path (right side). The expansive path is close to symmetric to the contracting path, which gives the network its u-shaped architecture. Compared to more traditional CNN's, the U-Net has proven to be successful even with less data to train on (Ronneberger et al., 2015).
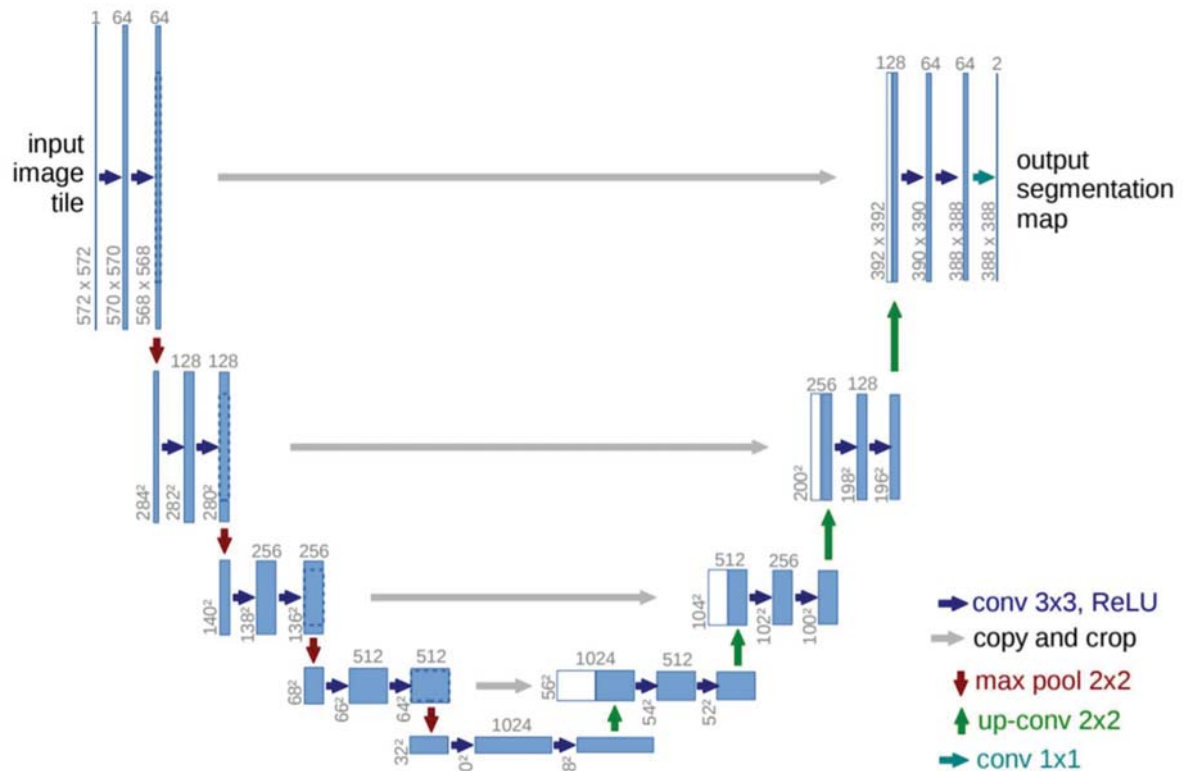
Figure 6. The U-Net architecture is named by the (almost) symmetrical contracting part (left) and expensive path (right). The green and blue arrows illustrate the 23 convolutions in the U-Net (Ronneberger et al., 2015)

The advances in machine learning open for faster and more generic workflows related to seismic processing and seismic interpretation. , Some recent publications on GAN's or cGAN's for seismic image to image translations include generalized seismic forward and inverse modeling (Mosser et al. 2019), translation from sketches to synthetic seismic images (Ferreira, 2019), low-quality migrated image to high-quality migrated image (Picetti et al., 2018) and migrated image to deconvolved reflectivity image (Picetti et al., 2018).

2.3 Geological settings of the datasets studied

In this thesis, we present generic methods for automated seismic interpretation applied on a range of datasets. The geological settings of these seismic datasets are still important as they allow us to evaluate and explain our results. Most of the datasets we have used are provided by Lundin Norway AS and cover areas in the SW Barents Sea north of Norway, near the Loppa High and the Polhem Subplatform. These areas have commercial interest as they contain the Alta, Gotha and Filicudi

discoveries by Lundin Norway AS and the Johan Castberg discovery by Equinor ASA. Figure 7 shows a regional map of the SW Barents Sea annotating the structural elements, such as the Loppa High and the Polhem Subplatform.
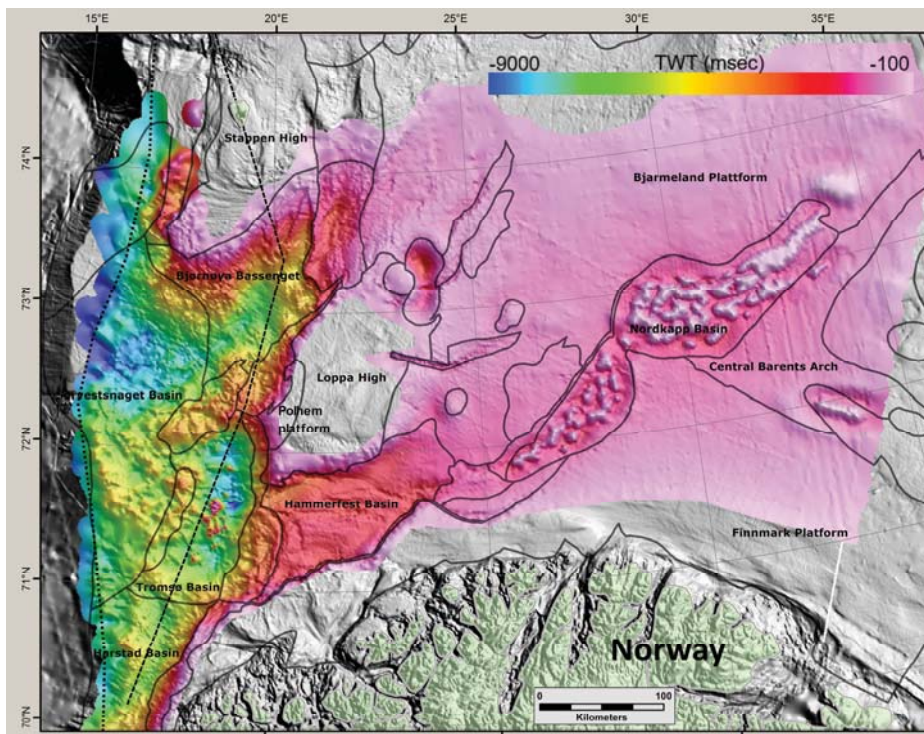
Figure 7. Regional map of the SW Barents Sea north of Norway, where the color bar indicates the depth of the Base Cretaceous Unconformity in TWT. The map shows structural elements such as the Loppa High and the Polhem Subplatform.

The SW Barents Sea has a complex geology with sedimentary packages ranging in age from Late Paleozoic to present and a history of crustal thinning through several rift phases that contributed to a series of rifting, subsidence, tilting, uplift, erosion and inversion events (Faleide et al., 1993; Breivik et al., 1998; Glørstad-Clark et al., 2010). These rift-phases have led to the formation of the basins and highs in the Barents Sea, such as the Loppa High (Gabrielsen et al., 1990, 1993; Faleide et al. 1993; Gudlaugsson et al., 1998; Glørstad-Clark et al., 2010).

The Loppa High was, prior to its inversion in the Early Cretaceous (Indrevær et al., 2017), a Mesozoic sedimentary depocenter with a strong sedimentary influx and accumulation of prograding deltaic wedges providing thick, mainly Triassic, successions across the area (Glørstad-Clark et al., 2010, 2011). Subsequent tectonic activity caused the Mesozoic strata to experience

normal faulting and fault block rotation in the Jurassic (Gabrielsen et al., 1990, 1993; Faleide et al., 1993). During Early Cretaceous uplift, the Loppa High became subaerially exposed and subjected to erosion (Wood et al. 1989; Faleide et al. 1993; Glørstad-Clark et al., 2010). As a consequence of the Early Cretaceous uplift, Jurassic and Cretaceous sedimentary beds are eroded and thin or absent on the Loppa High, while they thicken into the deeper basins surrounding it. The Cenozoic strata on the Loppa High include a thin layer of Quaternary glacial sediments, while Paleogene strata accumulated in the basins surrounding the high (Fiedler and Faleide, 1996).

The Polhem Subplatform is separated from the Loppa High by the Jason Fault Complex which defines the western flank of the Selis ridge, a late Paleozoic structure (Glørstad-Clark et al., 2011). Southwest of the Polhem Subplatform, the Ringvassøy-Loppa Fault Complex defines the transition into the Tromsø Basin (Gabrielsen et al., 1990), while the Bjørnøyrenna Fault Complex bounds the subplatform towards the Bjørnøya Basin in the northwest. The major faults on the Polhem Subplatform are in general extensional faults of Jurassic to early Cretaceous age, following the trends of the Polhem Subplatform boundary faults; the N-S trending Jason Fault Complex in the east, and the NW-SE trending Ringvassøy-Loppa Fault Complex in the west (Gabrielsen et al., 1993; Faleide et al., 1993; Glørstad-Clark et al., 2011). The N-S trend is believed to have been formed in Permian, and re-activated later in Mesozoic, and it continues north of the Polhem Subplatform along the eastern boundary fault of the Bjørnøya Basin and the western boundary fault of the Fingerdjupet Basin (Serck et al., 2017).

Figure 8 illustrates a 2D seismic image across the Loppa High where the stratigraphic sequences are manually outlined with different colors. Two major unconformities, annotated with black lines, are interpreted to be the Upper Regional Unconformity (URU) and the Base Cretaceous Unconformity (BCU).
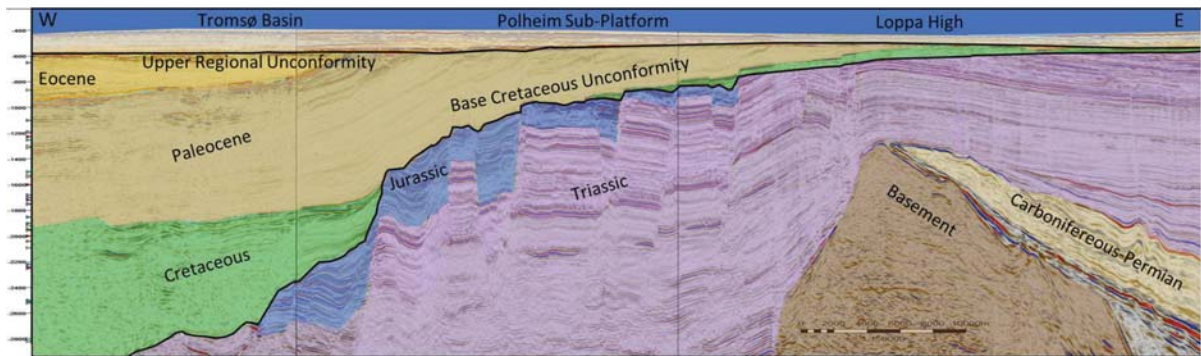
Figure 8. Manually outlined stratigraphic sequences superimposed onto a 2D seismic image of the Loppa High in the SW Barents Sea, north of Norway. Major unconformities are annotated with black lines, while the stratigraphic sequences are illustrated with unique colors.

The Base Cretaceous Unconformity (BCU) separates Paleocegne sediments from underlying pre-Cretaceous, Mesozoic sediments. The BCU is associated with several phases of uplift and erosion and is in many places a composite unconformity of the Base Cretaceous unconformity and the Base Paleocene unconformity. The upper regional unconformity (URU) developed in Quarternary time when glaciers eroded the Norwegian shelf. It is believed to have eroded 500-1000 m of section off the area around the Loppa High. Today the URU separates glacially derived Quarternary sediments from underlying pre-glacial Paleocene sediments deposited during the time the Atlantic Ocean opened between Norway and Greenland (Fiedler and Faleide, 1996; Dimakis et al., 1998).

Chapter 3. Summary and implications of papers

This chapter presents a summary of the papers this thesis consists of; two published peer-reviewed journal papers, one submitted, and one manuscript prepared for submission. In all of these, A. J. Bugge is the first author. The peer-reviewed journal papers and the submitted manuscripts are included in Chapter 6.

3.1 Paper I

The first paper covered in this thesis presents semi-automatic seismic interpretation based on image processing tools. The semi-automatic interpretation is presented through two independent methods, one on the identification and extraction of 3D unconformities, and one on 3D fault extraction and individualization. The proposed methods are implemented with a case-study on the well imaged Polhem Subplatform in the SW Barents Sea. The Polhem Subplatform has a complex structural geology with normal faults reactivated through several rift phases, and two major unconformities, the Upper Regional Unconformity and the Base Cretaceous Unconformity, which in some places is a composite unconformity with the Base Paleocene Unconformity.

3.1.1 Data

The conventional 8-80 Hz PSTM seismic data used in this case study covers most of the Polhem Subplatform covering approximately 120 km^2 with bin size 25 meters, and a (studied) record length of 3,5 seconds TWT. Two seismic attributes were extracted from the dataset. The attribute data included global 2D autotracked reflection data and fault likelihood data (Hale, 2013). The global 2D autotracked reflection data represent coherent seismic reflective interfaces and was generated with a seedless algorithm proprietary to Lundin Norway AS.

3.1.2 Summary

In this paper, unconformities were semi-automatically identified based on the assumption that the stratigraphic stacking patterns and the seismic amplitudes above and below an unconformity are significantly different. Instead of generating new attributes to highlight the unconformities (e.g. Barnes et al., 2000; Wu and Hale, 2015a; Qi et al., 2017), we used combined information from the available attribute data to extract detected unconformities as individual binary 3D surfaces.

To define a stacking pattern, reflections with similar orientation with a close distance to each other were grouped together. Next, Sobel edge-detection was applied on the seismic data in order to detect changes in the seismic amplitudes. Then, each stratigraphic stacking pattern was combined with the edge detection data to define one seismic sequence, meaning that one defined sequence had a stacking pattern and seismic amplitudes that in general differed from the sequences surrounding it. Finally, its top or base boundary was extracted and stored in a binary 3D matrix, assumed to represent an unconformity. Figure 9 shows 2D and 3D views of the Polhem Subplatform, where the proposed method has identified and extracted three surfaces; the seabed, the Upper Regional unconformity (URU) and the Base Cretaceous unconformity (BCU).
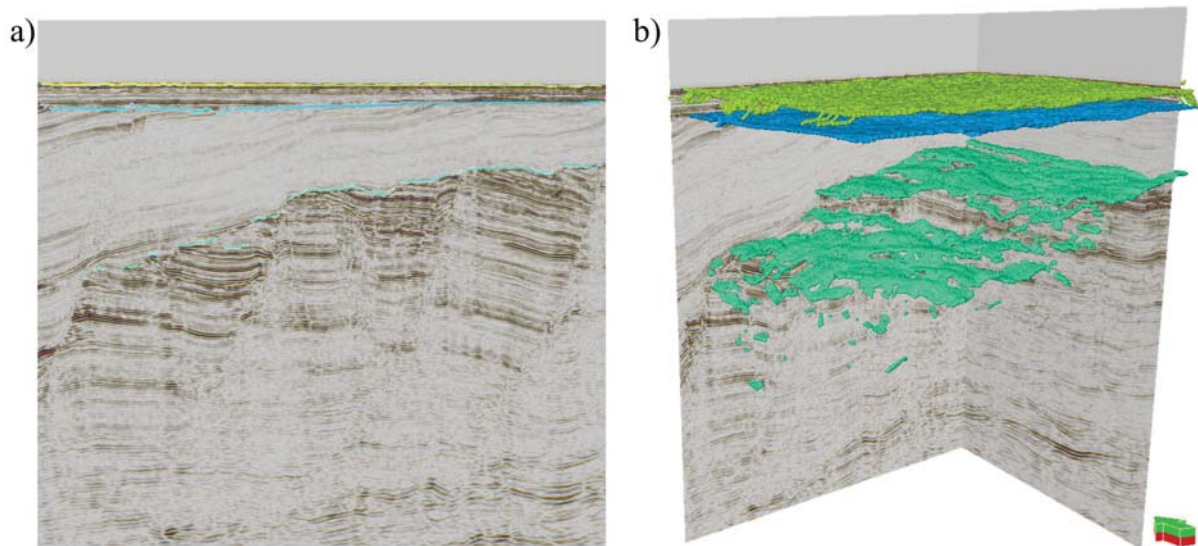

Figure 9. The figure shows a 2D and 3D view of three detected unconformities on the Polhem subplatform. In (b), each unconformity ha been exported to Petrel as individual ascii-files.

To separate and extract faults, we assumed that each fault surface could be targeted as a 3D object in a binary representation of the fault likelihood cube (Hale, 2013). Prior to this, intersecting faults were addressed using morphological filter operations and assigning the objects to different dip cubes. Objects that met a set of user-defined filter criteria related to fault size were extracted from each of the dip cubes. The separation of intersecting faults involved a series of 2D and 3D processing steps where the first step was to remove branch points within the cube. A branch point was defined where a pixel connected to 3-or-more neighboring pixels and the operation required infinitely thinned faults in time slice view. Next, objects were separated into dip cubes, where the measured dip of one assumed fault was defined as the measured 2D orientation of the main axis

of each object on a seismic line in relation to the x-axis of the line. The new dip cubes then consisted of 3D objects dipping in similar direction and assumed fault surfaces were extracted individually from each dip cube (Figure 10).
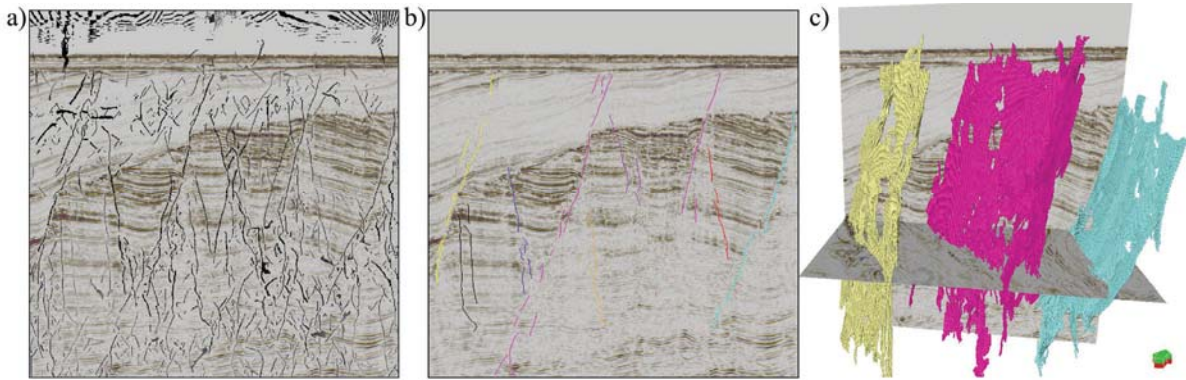
Figure 10. This figure shows (a) a 2D line of the Fault likelihood attribute superimposed onto the seismic data covering the Polhem Subplatform, (b) a 2D line of the semi-automatically extracted 3D faults after application of the method proposed in this paper, and (c) a 3D view of three large faults extracted and exported to Petrel.

3.2 Paper II

In this paper, we present a data-driven three-dimensional method to automatically correlate, track and extract seismic horizons from seismic volumes. The method uses non-local dynamic time warping to simultaneously correlate multiple seismic events. Because the method does not require manually picked seed points or prior structural restoration, it does not rely on interpretive experience or geological knowledge. With different case examples, the proposed method was used to extract seismic horizons from real 3D seismic volumes containing well imaged but complex structures such as heavily faulted successions and rotated fault blocks.

3.2.1 Data

The case examples included in this paper are (1) Triassic successions on the Loppa High with large Jurassic normal faults, (2) Rotated fault blocks on the Polhem Sub-platform and (3) a subset from the open-source data Netherlands F3 with salt intrusions and a few major faults. The Loppa High 3D seismic data are PSTM TopSeis™ data from the first ever marine source-over-cable acquisition (Lie et al., 2018) with bandwidth 4-110 Hz. The Polhem data are conventional 8-80 Hz PSTM seismic data. The Netherlands F3 data from the North Sea offshore Netherlands are provided by

dGB Earth Sciences B.V. through OpendTect. The subset used in this paper covers a vertical range from 0.8 to 1.8 s.

3.2.2 Summary

Dislocated and truncated horizons in seismic images cause difficulties for both manual and automatic interpretation. The method proposed in this paper correlates seismic horizons across discontinuities and does not require user input in the form of seed points or prior identification of faults. Furthermore, the method is robust towards amplitude changes along a seismic horizon and does not change polarity from peak to trough or vice versa.

To extract horizons from 3D seismic images, we set up a grid of seismic traces, and use a large sliding window to iteratively match every pair of the gridded traces at all window locations. The grid step and the window size are key parameters for this operation, and it is crucial to ensure that enough traces are represented on each side of a discontinuity within a window for optimal correlation of displaced horizons. The sliding window matches full-length seismic traces using non-local dynamic time warping to extract grids of correlated points for target horizons. We can correlate horizon grids for any number of target horizons simultaneously. (Figure 11).
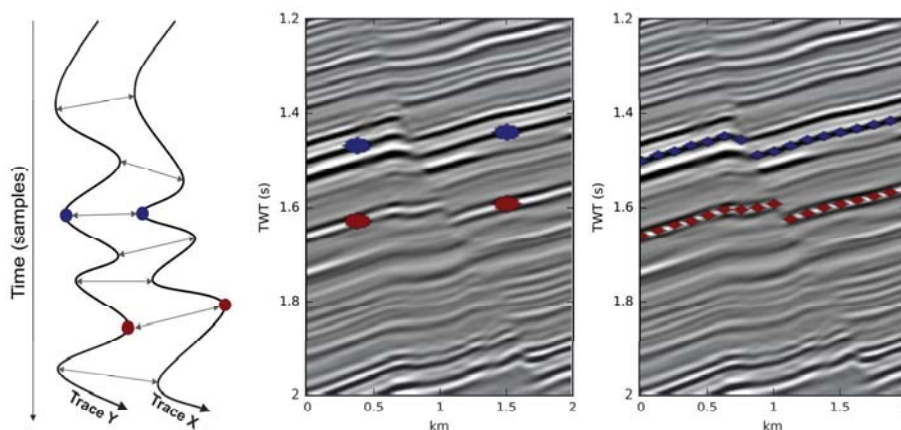
Figure 11. The figure illustrates two reflector events, annotated with red and blue dots, superimposed onto a small offset faulted seismic image. The reflectors are correlated using dynamic time warping.

Since the sliding window iteratively matches seismic traces, each trace will be re-visited multiple times and this iterative process may produce several possible locations for a reflective event in the correlated grids. We exploit this iterative process to record an uncertainty measure for each grid

point and to keep the most accurate correlations and discard less-accurate ones. The accuracy measurement is a calculated relationship between how many times a trace is re-visited and how many of these re-visitations provide the same location for a point along a target horizon.

Each horizon grid is interpolated using a linear interpolation approach (curve fitting) between neighboring correlated points, where an implemented phase constraint only allows interpolation when the unwrapped phase values are continuous. This results in interpolation along coherent segments of the horizons, where the reflective event consistently follows a peak or trough, and no interpolation across faults or other disruptions in the seismic image (Figure 12). The implementation of this constraint will therefore discard potential outliers in the correlated horizon grid.
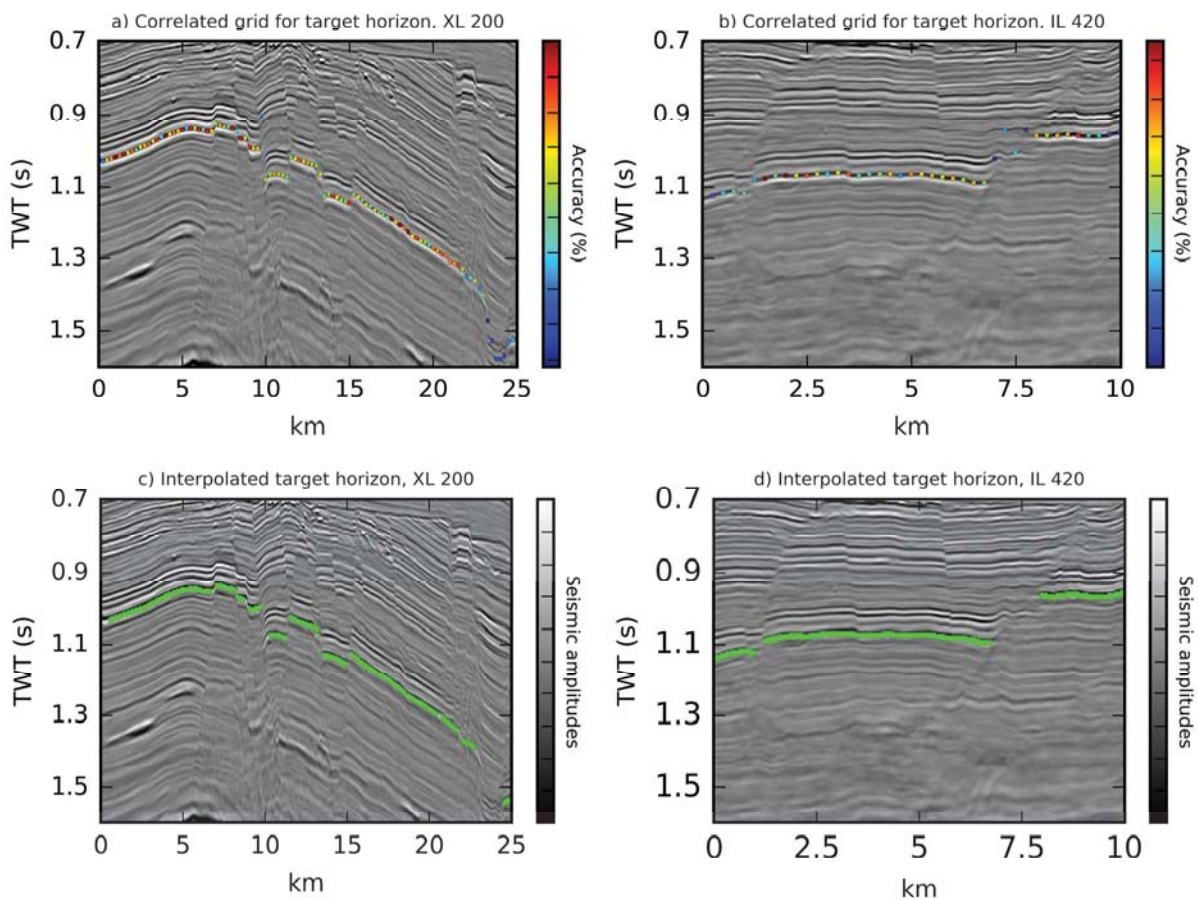

Figure 12. The figure shows inline and crossline views for one correlated target horizon in a heavily faulted seismic image from the SW Barents Sea before (a, b) and after (c, d) interpolation. The color bars in (a) and (b) illustrate correlation accuracy.

3.3 Paper III

Paper III presents a data-driven method for first-order identification of major stratigraphic units in 3D seismic images. With this method we introduce a new 3D texture descriptor for seismic data and a new way of computing feature vectors that describe seismic stratigraphy for given seismic sub-volumes. The motivation behind this work was to automate different interpretation and processing tasks, such as to constrain horizon tracking for better automated correlation of seismic horizons and to roughly outline structure in initial models for seismic inversion.

3.3.1 Data

The proposed method is applied on modern broadband 3D seismic data covering the Loppa High, where the stratigraphy includes Caledonian basement rocks and sedimentary packages from Late Paleozoic to present. The Loppa High data are 4-110 Hz PSTM TopSeis™ data (Lie et al., 2018) that covers 1000 inlines and 400 crosslines laterally and 3 seconds TWT vertically. In order to illustrate robustness of the method, we also tested it on another 3D PSDM dataset over the Utsira High in the North Sea.

3.3.2 Summary

To automatically identify stratigraphic units, we assume that seismic sequences honor a layer-cake model of the earth with layers that can be discriminated by their differences in seismic amplitudes and texture. First, we compute feature vectors that represent the amplitudes, texture and depth for given 3D sub-cubes from the seismic data. In order to describe the seismic texture, a new texture descriptor that quantifies a 3D binary pattern around each pixel in the seismic data is proposed. The feature vectors are then preprocessed and clustered using the HDBSCAN algorithm (Campello et al., 2013). The HDBSCAN is an unsupervised machine learning algorithm based on the DBSCAN algorithm proposed by Ester et al. (1996). With the HDBSCAN, a hierarchy of all possible DBSCAN solutions for all possible cluster density thresholds is constructed, and clusters are condensed from this hierarchy based on a minimum cluster size. We assume that each condensed cluster represents one stratigraphic unit with relatively conformable seismic reflections (Figure 13). Filling of holes and removal of small mis-labelled and mis-placed patches is done with binary morphological operations by removal of objects that are significantly smaller than the

connected identified clusters. The assumed boundaries are smoothed with a Savitzky-Golay filter; a digital low-pass filter that increases signal to noise ratio without distorting the original signal too much.
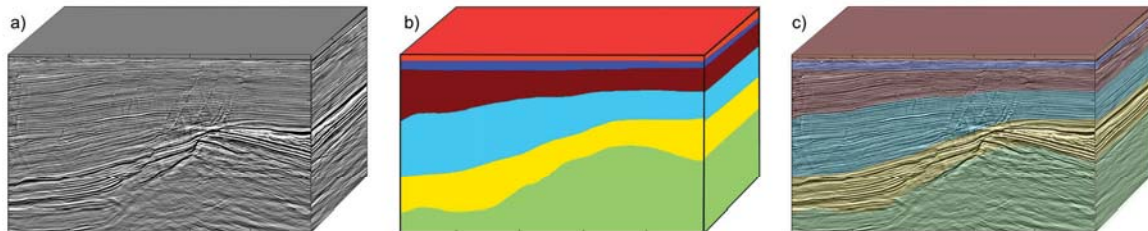

Figure 13. The figure shows a seismic cube (a), final identified stratigraphic units using the proposed method in this paper, and (c) the Identified units superimposed onto the input seismic cube.

With a prior identification of stratigraphic units, we perform constrained automatic horizon tracking within targeted seismic units (Figure 14). Each target unit is constrained using the upper and lower boundary of the identified unit, and in order to correlate seismic horizons we use the non-local dynamic time warping approach described in Paper II.
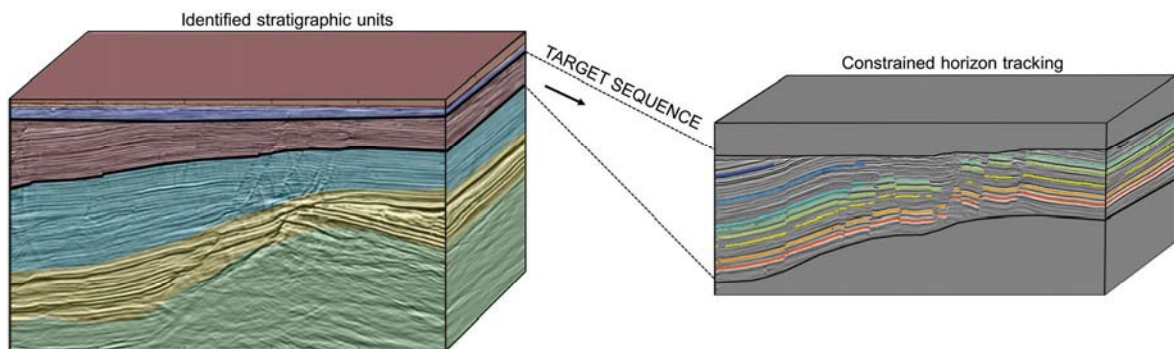
Figure 14. The figure shows automatically correlated seismic horizons within a constrained seismic unit. The constrained unit is identified with the method proposed in this paper, and the seismic horizons are tracked with the approach described in Paper II. The combination of these methods allows us to automatically interpret seismic horizons in structurally and stratigraphically complex seismic volumes.

3.4 Paper IV

This paper utilizes the methods proposed in Paper I, II and III, and introduces the use of conditional generative adversarial networks (cGAN's) in order to discuss key aspects of an automated seismic interpretation workflow. These aspects include:

(1) Seismic quality improvement using a cGAN

(2) Identification and individualization of faults using a cGAN and
    image processing.

(3) Identification of stratigraphic units with hierarchical clustering

(4) Horizon tracking using dynamic time warping

3.4.1 Data

The paper presents a range of case examples on a variety of real seismic datasets provided by Lundin Norway AS in the SW Barents Sea and in the North Sea.

3.4.2 Summary

Here, we use both supervised and unsupervised machine learning, together with image processing and signal processing to discuss some of the key aspects with automated seismic interpretation. First, we introduce the use of conditional generative adversarial networks for both seismic image quality improvement and fault detection. Further, we implement the fault individualization technique from Paper I, the multi-horizon tracking method from Paper II and the stratigraphic unit identification from Paper III, and we show how these methods can be combined in order to extract information on the timing and orientation of faults and to generate wheeler seismic.

Seismic quality is an important limiting factor when interpreting seismic data, and the notion of improving seismic image-quality can be a time consuming process consisting of many steps and re-tuning of parameters. Here, we show the use of a modified cGAN in order to automate the process of improving the seismic quality and reduce the time spent on seismic processing (Figure 15).
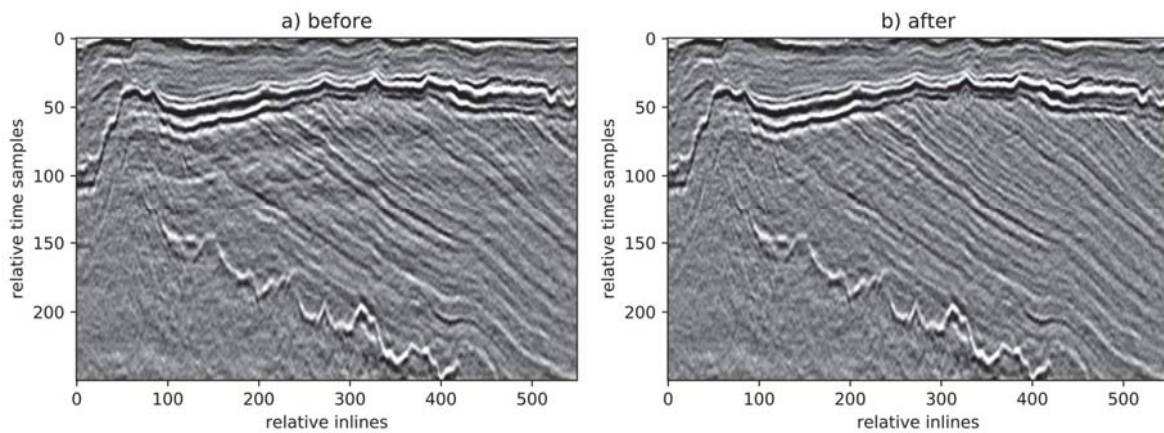
Figure 15. A seismic section before (a) and after (b) image to image translation. Here a cGAN is trained improve the signal-to-noise ratio. This figure shows a 2D slice from a large 3D seismic volume from the North Sea. Note how the low frequency near-horizontal multiples crossing the dipping section are attenuated on the right image

Further, we train a cGAN to translate from seismic images to fault likelihood images and use the method from Paper I to extract individual 3D fault surfaces from the fault likelihood images. The method from Paper I also allows us to simultaneously extract information, or filter the faults, based on specific features related to e.g. orientation or time of last reactivation (Figure 16). This may be of relevance to the interpreter to help understand timing and importance of different tectonic phases.
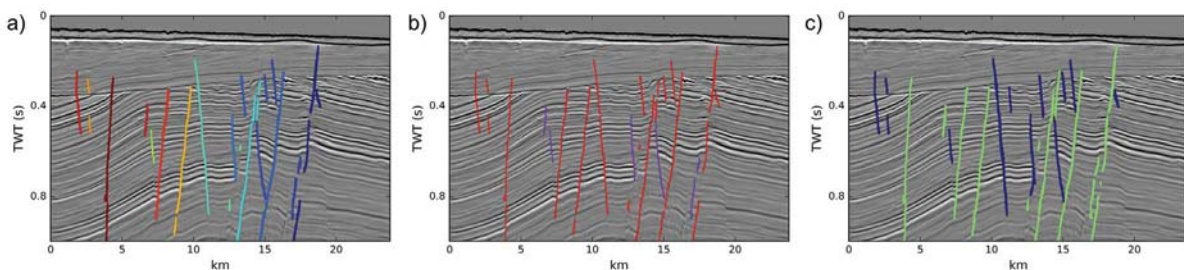
Figure 16. (a) A 2D view of filtered and individualized 3D faults, (b) faults filtered into two phases of activity, older (purple) and younger (red), and (c) fault separated into two dip orientations, positive (red) and negative (blue).

Wheeler seismic is produced by considering interpreted surfaces as snapshots of geologic time linked with transit cycles of the base level. The base level can be regarded as an ultimate 'time' reference for stratigraphic units. Here, we generate wheeler seismic by flattening each identified stratigraphic sequence on a target horizon within each unit. Figure 17 shows all the identified

stratigraphic sequence (a) before flattening, and (b) after flattening to produce wheeler seismic which illustrates missing sections and time gaps. This operation is an effective way of validating both the stratigraphic unit identification and the horizon tracker. More importantly, this is a step towards generating automated wheeler seismic, which can provide important information when trying to understand the evolution of the subsurface.
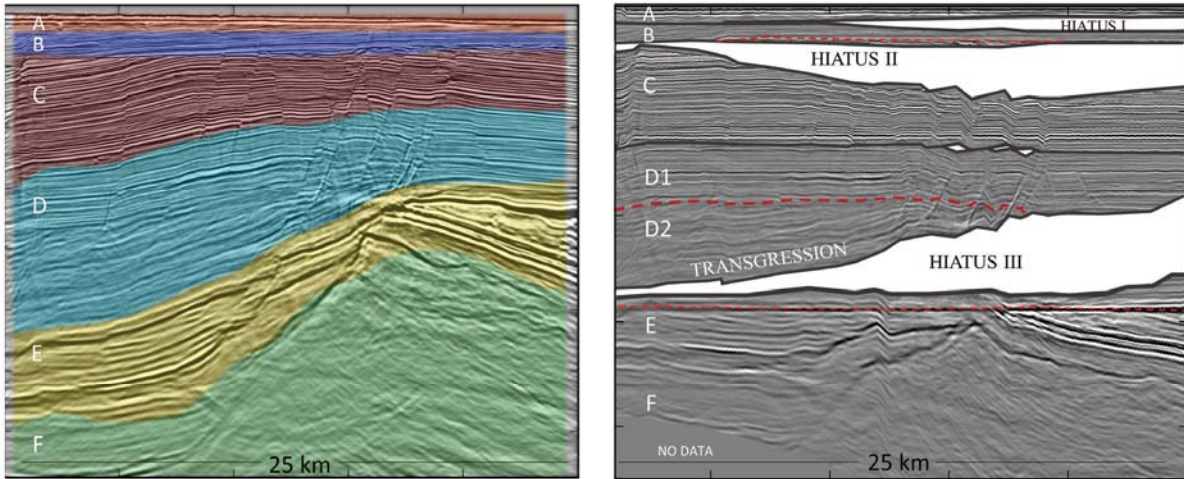
Figure 17. By automatically identifying stratigraphic units (a), and then performing constrained horizon tracking within each unit, we can flatten key seismic horizons within each of the identified units to generate wheeler seismic (b). In (a), each identified sequence is labelled with a letter, and in (b), we have annotated candidate disconformities and unconformities not detected or not accurately delineated with our method with dashed red lines.

Chapter 4. Concluding remarks and Outlook

In this thesis, we have presented data-driven methods towards automated seismic interpretation through four papers. This chapter presents some concluding remarks related to these papers and suggestions for further research.

4.1 Concluding remarks

Automated seismic interpretation is a broad topic; In this thesis, we have focused on the identification and extraction of features from seismic data, such as faults, unconformities, seismic horizons and discrete stratigraphic sequences. The common objective in **Paper I**, **II**, **III** and **IV** was to automate the state-of-the art seismic interpretation workflow.

Paper I introduced semi-automatic methods for extracting unconformities and faults from seismic data using image processing tools. With the method for unconformity extraction, we identified noncoherent unconformities on the Polhem Subplatform in the SW Barents Sea. Further, we individualized, filtered and extracted major normal faults in the same area with our method for fault extraction. In contrast to other seismic attributes and methods that highlight different seismic features, the most important outcome of this paper was that the methods we proposed allow for extraction of unconformities and faults as individual 3D objects. In **Paper IV**, we used the method for fault individualization to automatically obtain information of fault timing, orientation and different tectonic phases.

In **Paper II** we proposed a 3D data-driven method to correlate and extract seismic horizons across structurally complex geological settings. This new method uses pattern recognition to correlate multi-horizons simultaneously, which proved to be robust with regards to horizons dislocated by faults. Because dislocated horizons can be correlated and tracked without any manually selected seed points or any prior structural restoration, the proposed method does not rely on interpretive experience or geological knowledge (provided the seismic image quality is good enough)

Paper III is a continuation of **Paper II**. In **Paper II** we showed that the data-driven multi-horizon tracker benefitted from the implementation of stratigraphic constraints, specifically when constraining the horizon tracker within relatively conformable stratigraphic units. Therefore, in

Paper III, we proposed a method to automatically identify major first-order stratigraphic units in 3D seismic data. This is a composite method consisting of several steps, where we (1) introduce a new 3D texture attribute, (2) compute feature vectors that describe the seismic texture, amplitudes and two-way travel time, and (3) structure and group these feature vectors into assumed stratigraphic units using unsupervised machine learning. A limitation with this method is that, while it does identify major stratigraphic units, it does not (yet) accurately delineate the actual sequence boundaries that separate them.

Paper IV discusses elements and consequences of data-driven seismic interpretation, both through utilization of the methods proposed in **Paper I**, **II** and **III**, and by introducing the use of conditional generative adversarial networks for seismic image quality improvement (e.g. multiple removal) and fault attribute generation. Further, **Paper IV** uses these methods to automatically extract information on fault timing and fault orientation, as well as to generate wheeler seismic. These are steps towards an automated interpretive workflow where, ideally, the interpreter is given more time to analyze and interpret, without having to first manually map and extract data.

4.2 Outlook

Chapter 2 discussed the scientific background relevant for the research presented in this thesis. However, there has been a rapid evolution in automated seismic interpretation occurring in parallel to our work, particularly with the use of machine learning. Consequently, both research papers and commercial products for automated seismic interpretation have been introduced and developed since the initiation of this Ph.D study. Among the seismic features that we cover in this thesis, fault interpretation has showed particularly successful results using machine learning. Typically, these new fault identification methods use supervised machine learning trained either on manually interpreted faults or on synthetic seismic data. Several of these show that when trained on a significant amount of data, the networks are able to successfully identify faults in new unseen datasets more successfully than state-of-the art fault attributes (Huang et al., 2017; Di et al., 2018; Guitton, 2018; Guo et al., 2018; Larsen et al., 2018, Zhao and Mukhopadhyay, 2018; Wu et al., 2018, and Wu et al., 2019). The most recent method for fault identification provided by Wu et al. (2019) (FaultSeg3D) uses an end-to-end CNN to detect faults from 3D seismic images. With a simplified U-net architecture (Ronneberger et al., 2015), they train on 3D synthetic seismic images

and corresponding labelled fault images. Although trained on synthetic data, the network successfully identifies faults in unseen seismic volumes.

Based on the results from this Ph.D. research, we present suggestions for further work to optimize the methods developed in this thesis:

- To further improve the fault individualization introduced in **Paper I**, we suggest combining this method with more recent advances in fault identification (e.g. the FaultSeg3D proposed by Wu et al., 2019). In **Paper I**, we showed individualization and extraction of 3D fault surfaces from a fault likelihood attribute (Hale, 2013). Since this, new machine learning-based methods for fault identification have proved more successful than state-of-the art fault attributes (Guo et al., 2018; Zhao and Mukhopadhyay, 2018; Wu et al., 2018, Larsen et al., 2018 and Wu et al., 2019). However, even with the recent advances in fault identification, few new attempts have yet been made in order to extract individual fault surfaces and this opens for new research potential.

- To optimize the correlative multi-horizon tracker presented in **Paper II**, we suggest that an automatically adaptive window size can be implemented by constraining the horizon tracker to both identified (as in **Paper III**) and *classified* stratigraphic units. The horizon tracker from **Paper II** showed robustness towards faults and discontinuities, however, this required a large window size for the sliding window. With a large window size, the computing time increases, especially if the window is not vertically constrained. We suggest further work on this method that involves an adaptive window size that can automatically decrease in areas with flat or dipping non-faulted reflectors and increase when the structural complexity increases. With this implementation, we also suggest that the window size should be decreased, particularly when horizons are correlated in non-faulted prograding stratigraphy if the number of reflectors changes rapid laterally. An alternative to an adaptive window size could be to dynamically re-sample the seismic data or the seismic unit to fit the window size.

- In **Paper IV**, we combine information from automatically extracted seismic features to generate wheeler volumes and to structure information on fault timing and fault orientation.

We hope that this work is considered a step towards an automated dynamic tectono-stratigraphic seismic restoration. Whereas traditional seismic reconstruction uses manually interpreted reference horizons and faults, we propose to implement our methods for 3D horizon correlation (**Paper II**) and 3D fault extraction and individualization (**Paper I**) to speed up and automate this process. It is also likely that our method for identification of stratigraphic units (**Paper III**) could be implemented in this process. As our methods allows for 3D extraction of faults, horizons and stratigraphic units, they can be used in a 3D structural restoration.

The recent advances in automated seismic interpretation indicate that there is a huge potential in the integration of data science and geoscience. As the industry continues to focus on the implementation of digital tools into geophysical workflows, we will continue to see a range of new AI-driven solutions for seismic interpretation. Particularly U-Net's and GAN's have proven to be very efficient machine learning tools for seismic interpretation with high success rates even when trained on limited training data. With an extensive focus on faults the last few years, we hope to see more focus on supervised machine learning for automatic interpretation of other seismic features as well, such as seismic horizons, unconformities and stratigraphic sequence patterns such as onlaps, downlaps and truncations.

Chapter 5. References

Badley, M.E., 1985. Practical seismic interpretation. International Human Resources Development Corporation, p. 266.

Bahorich, M., Farmer, S., 1995. 3-D seismic discontinuity for faults and stratigraphic features: The coherence cube. The Leading Edge 1053–1058.

Bakker, P., 2002. Image structure analysis for seismic interpretation. Delft University of Technology.

Barnes, A.E., 2000. Attributes for automating seismic facies analysis. SEG Technical Program Expanded Abstracts 553–556.

Breivik, A.J., Faleide, J.I., Gudlaugson, S.T., 1998. Southwestern Barents Sea margin: late Mesozoic sedimentary basins and crustal extension. Tectonophysics 21–44.

Campello, R., Moulavi, D., Sander, J., 2013. Density-Based Clustering Based on Hierarchical Density Estimates. Presented at the Pacific-Asia Conference on Knowledge Discovery and Data Mining, Springer. https://doi.org/10.1007/978-3-642-37456-2_14

Chopra, S., 2002. Coherence Cube and beyond. first break 20–33, 27.

de Matos, M.C., Osorio, P.L.M., Johann, P.R.S., 2007. Unsupervised seismic facies analysis using wavelet transform and self-organizing maps. Geophysics 72, P9–P21.

Di, H., Gao, D., 2016. Improved estimates of seismic curvature and flexure based on 3D surface rotation in the presence of structure di. GEOPHYSICS 81, 13–23.

Di, H., Wang, Z., AlRegib, G., 2018. Deep convolutional neural networks for seismic salt-body delineation. Presented at the American Association of Petroleum Geologists (AAPG), Annual Convention and Exhibition (ACE), Salt Lake City.

Dimakis, P., Braathen, B.I., Faleide, J.I., Elverhøi, A., Gudlaugsson, S.T., 1998. Cenozoic erosion and the preglacial uplift of the Svalbard–Barents Sea region. Tectonophysics 300, 311–327.

Ester, M., Kriegel, H.-P., Sander, J., Xu, X., 1996. Density-Based Algorithm for Discovering Clusters in Large Spatial Databases with Noise. Proceedings of the Second International Conference on Knowledge Discovery and Data Mining 226–231.

Faleide, J.I., Vagnes, E., Gudlaugson, S.T., 1993. Late Mesozoic-Cenozoic evolution of the south-western Barents Sea in a regional rift-shear tectonic setting. Marine and Petroleum Geology 10, 186–214.

Ferreira, R., Oliveira, D., Vital Brazil, E., 2019. Synthetic Seismic Images from Simple Sketches Using Deep Generative Networks. Presented at the 80th EAGE Conference and Exhibition.

Fiedler, A., Faleide, J.I., 1996. Cenozoic sedimentation along the southwestern Barents Sea margin in relation to uplift and erosion of the shelf. Global and Planetary Change 12, 75–93.

Gabrielsen, R.H., Færseth, R., Jensen, L.N., Kalheim, J.E., Riis, F., 1990. Structural elements of the NCS Part I: The Barents Sea Region. NPD-bulletin.

Gabrielsen, R.H., Grunnaleite, I., Ottesen, S., 1993. Reactivation of fault complexes in the Loppa High area, southwestern Barents Sea. Norwegian Petroleum Society Special Publications 631–641.

Gersztenkorn, A., Marfurt, K.J., 1999. Eigenstructure-based coherence computations as an aid to 3-D structural and stratigraphic mapping. GEOPHYSICS, 64, 1468–1479.

Glørstad-Clark, E., Birkeland, E.P., Nystuen, J.P., Faleide, J.I., Midtkandal, I., 2011. Triassic platform-margin deltas in the western Barents Sea. Marine and Petroleum Geology 28, 1294–1314.

Glørstad-Clark, E., Faleide, J.I., Lundschien, B.A., Nystuen, J.P., 2010. Triassic seismic sequence stratigraphy and paleogeography of the western Barents Sea area. Marine and Petroleum Geology 27, 1448–1475.

Goodfellow, I., Pouget-Abadie, J., Mirza, M., Xu, B., Warde-Farley, D., Ozair, S., Courville, A., Bengio, Y., 2014. Generative adversarial nets. NIPS.

Gudlaugson, S.T., Faleide, J.I., Johansen, S.E., Breivik, A.J., 1998. Late Palaeozoic structural development of the South-western Barents Sea,. Marine and Petroleum Geology 15, 73–102.

Guitton, A., 2018. 3D convolutional neural networks for fault interpretation. Presented at the 80th Annual International Conference and Exhibition, EAGE, Extended Abstracts.

Guo, B., Li, L., Luo, Y., 2018. A new method for automatic seismic fault detection using convolutional neural network. Presented at the 88th Annual International Meeting, SEG, Expanded Abstracts, pp. 1951–1955.

Hale, D., 2013. Methods to compute fault images, extract fault surfaces, and estimate fault throws from 3D seismic images. GEOPHYSICS 78, 33–43.

Hoek, T., Gesbert, S., Pickens, J., 2010. Geometric attributes for seismic stratigraphic interpretation. The Leading Edge 1056–1065.

Huang, L., Dong, X., Clee, T.E., 2017. A scalable deep learning platform for identifying geologic features from seismic attributes. The Leading Edge 36, 249–256. https://doi.org/http://dx.doi.org/10.1190/tle360300249.1

Indrevær, K., Gabrielsen, R.H., Faleide, J.I., 2017. Early Cretaceous synrift uplift and tectonic inversion in the Loppa High area, southwestern Barents Sea, Norwegian shelf. Journal of the Geological Society 174, 242–254. https://doi.org/10.1144/jgs2016-066

Isola, P., Zhu, J.-Y., Zhou, T., Efros, A.A., 2017. Image-to-Image Translation with Conditional Adversarial Networks, in: IEEE Conference on Computer Vision and Pattern Recognition (CVPR).

Larsen, E., Purves, S.J., Economou, D., Alaei, B., 2018. Is Machine Learning taking productivity in petroleum geoscience on a Moore's Law trajectory? First Break 36, 135–141.

Lie, J.E., Danielsen, V., Dhelie, P.E., Sablon, R., Siliqi, R., Grubb, C., Vinje, V., Soubaras, R., 2018. A novel source-over-cable solution to address the Barents Sea imaging challenges. Presented at the Marine Acquisition Workshop 2018, Oslo, Norway, pp. 1–5.

Lomask, J., Guitton, A., Fomel, S., Claerbout, J., Valenciano, A.A., 2006. Flattening without picking. Geophysics 71, P13–P20. https://doi.org/10.1190/1.2210848

Marfurt, K.J., Kirlin, R.L., Farmer, S.L., Bahorich, M.S., 1998. 3-D seismic attributes using a semblance-based coherency algorithm. GEOPHYSICS 63, 1150–1165.

Mitchum, R.M.J., Vail, P.R., Thompson, S.I., 1977. Seismic Stratigraphy and Global Changes of Sea Level, Part 2: The Depositional Sequence as a Basic Unit for Stratigraphic Analysis. https://doi.org/https://doi.org/10.1306/M26490C4

Mosser, L., Kimman, W., Dramsch, J., Purves, S., De la Fuente Briceño, A., Ganssle, G., 2018. Rapid seismic domain transfer: Seismic velocity inversion and modeling using deep generative neural networks. Presented at the 80th EAGE Conference and Exhibition.

Pedersen, S.I., Randen, T., Sønneland, L., Steen, Ø., 2002. Automatic fault extraction using artificial ants. SEG Int'l Exposition and 72nd Annual Meeting.

Pedersen, S.I., Skov, T., Hetlelid, A., Fayemendy, P., Randen, T., Sønneland, L., 2003. New paradigm of fault interpretation. Schlumberger Stavanger Research.

Picetti, F., Lipari, V., Bestagini, P., Tubaro, S., 2018. A generative-adversarial network for seismic-imaging applications. SEG Technical Program Expanded Abstracts 2231–2235.

Qayyum, F., Betzler, C., Catuneanu, O., 2018. Space-time continuum in seismic stratigraphy: Principles and norms. Interpretation 6.

Qayyum, F., Betzler, C., Catuneanu, O., 2017. The Wheeler diagram, flattening theory, and time. Marine and Petroleum Geology 86, 1417–1430.

Qi, J., Lin, T., Zhao, T., Li, F., Marfurt, K.J., 2016. Semisupervised multiattribute seismic facies analysis. Interpretation 4, SB91-SB106.

Roberts, A., 2001. Curvature Attributes and their Application to 3D Interpreted Horizons. First Break 19, 85–100.

Roden, R., Smith, T., Deborah Sacrey, 2015. Geologic pattern recognition from seismic attributes: Principal component analysis and self-organizing maps. Interpretation 3, 59–83.

Roden, R., Smith, T., Santogrossi, P., Sacrey, D., Jones, G., 2017. Seismic interpretation below tuning with multi-attribute analysis. The Leading Edge 36, 330–339.

Ronneberger, O., Fisher, P., Brox, T., 2015. U-net: Convolutional networks for biomedical image segmentation. MICCAI.

Sakoe, H., Chiba, S., 1978. Dynamic Programming Algorithm Optimization for Spoken Word Recognition. IEEE TRANSACTIONS ON ACOUSTICS, SPEECH, AND SIGNAL PROCESSING ASSP-26, 43–49.

Serck, C.S., Faleide, J.I., Braathen, A., Kjølhamar, B., Escalona, A., 2017. Jurassic to Early Cretaceous basin configuration(s) in the Fingerdjupet Subbasin, SW Barents Sea. Marine and Petroleum Geology 86, 874–891. https://doi.org/http://dx.doi.org/10.1016/j.marpetgeo.2017.06.044

Stark, T.J., 2005. Generating a seismic Wheeler volume. Presented at the 75th Annual International Meeting, SEG, Expanded Abstracts, pp. 782–785.

Stark, T.J., 2003. Unwrapping instantaneous phase to generate a relative geologic time volume. Presented at the 73rd Annual International Meeting, SEG, Expanded Abstracts, pp. 1707–1710.

Taner, M.T., Koehler, F., Sheriff, R.E., 1979. Complex seismic trace analysis. Geophysics 44, 1041–1063.

Torabi, A., Alaei, B., Kolyukhin, D., Libak, A., Gabrielsen, R.H., Braathen, A., 2016. Fault geometric and seismic attributes; an integrated study with focus on the Barents Sea. first break 34, 51–58.

Vail, P.R., Mitchum, R.M.J., Todd, R.G., Widmier, J.M., Thompson, S.I., Sangree, J.B., Bubb, J.N., Hatlelid, W.G., 1977. Seismic Stratigraphy and Global Changes of Sea Level1.

Waldeland, A.U., Jensen, A.C., Gelius, L.-J., Solberg, A., 2018. Convolutional neural networks for automated

seismic interpretation. The Leading Edge 37, 529–537.

Wheeler, H.E., 1958. Time-stratigraphy. Am. Assoc. Petrol. Geol. Bull. 42 1047–1063.

Wood, R.J., Edrich, S.P., Hutchison, I., 1989. Influence of North Atlantic tectonics on the large-scale uplift of the Stappen High and Loppa High, western Barents Shelf. In: Tankard, A.J. & Balkwill, H.R. (eds) Extensional Tectonics and Stratigraphy of the North Atlantic Margins. AAPG Memoirs 46, 559–566.

Wu, X., Fomel, S., 2018. Least-squares horizons with local slopes and multigrid correlations. Geophysics 83, IM29-IM40. https://doi.org/10.1190/geo2017-0830.1

Wu, X., Hale, D., 2016a. Automatically interpreting all faults, unconformities, and horizons from 3D seismic images. Interpretation 4, T227--T237. https://doi.org/https://doi.org/10.1190/INT-2015-0160.1

Wu, X., Hale, D., 2016b. Moving faults while unfaulting 3D seismic images. Geophysics 81, 25–33.

Wu, X., Hale, D., 2015a. 3D seismic image processing for unconformities. Geophysics 80, IM35–IM44. https://doi.org/10.1190/geo2014-0323.1

Wu, X., Hale, D., 2015b. Horizon volumes with interpreted constraints. Geophysics 80, IM21-IM33.

Wu, X., Janson, X., 2017. , Directional structure tensors in estimating seismic structural and stratigraphic orientations. Geophysical Journal International 210, 534–548.

Wu, X., Liang, L., Shi, Y., Fomel, S., 2019. FaultSeg3D: Using synthetic data sets to train an end-to-end convolutional neural network for 3D seismic fault segmentation. GEOPHYSICS 84, IM35-IM45.

Wu, X., Shi, Y., Fomel, S., Liang, L., 2018. Convolutional neural networks for fault interpretation in seismic images. Presented at the : 88th Annual International Meeting, SEG, Expanded Abstracts, pp. 1946–1950.

Wu, X., Zhong, G., 2012. Generating a relative geologic time volume by 3D graph-cut phase unwrapping method with horizon and unconformity constraints. Geophysics 77, O21–O34. https://doi.org/10.1190/geo2011-0351.1

Zhao, T., 2018. Seismic facies classification using different deep convolutional neural networks. Presented at the SEG International Exposition and 88th Annual Meeting, pp. 2046–2050.

Zhao, T., Jayaram, V., Roy, A., Marfurt, K.J., 2015. A comparison of classification techniques for seismic facies recognition. Interpretation 3, SAE29–SAE58.

Zhao, T., Mukhopadhyay, P., 2018. A fault-detection workflow using deep learning and image processing. Presented at the 88th Annual International Meeting, SEG, Expanded Abstracts, pp. 1966–1970.

Chapter 6. Papers

Check for updates

A case study on semiautomatic seismic interpretation of unconformities and faults in the southwestern Barents Sea

Aina J. Bugge[1], Stuart R. Clark[2], Jan E. Lie[3], and Jan I. Faleide[4]

Abstract

Recently, there has been a growing interest in automatic and semiautomatic seismic interpretation, and we have developed methods for extraction of 3D unconformities and faults from seismic data as alternatives to conventional and time-consuming manual interpretation. Our methods can be used separately or together, and they are time efficient and based on easily available 2D and 3D image-processing algorithms, such as morphological operations and image region property operations. The method for extraction of unconformities defines seismic sequences, based on their stratigraphic stacking patterns and seismic amplitudes, and extracts the boundaries between these sequences. The fault-extraction method extracts connected components from a coherence-based fault-likelihood cube where interfering objects are addressed prior to the extraction. We have used industry-based data acquired in a complex geological area and implemented our methods with a case study on the Polhem Subplatform, located in the southwestern Barents Sea north of Norway. For this case study, our methods result in the extraction of two unconformities and twenty-five faults. The unconformities are assumed to be the Base Pleistocene, which separates preglacial and postglacial Cenozoic sediments, and the Base Cretaceous, which separates the severely faulted Mesozoic strata from prograding Paleocene deposits. The faults are assumed to be mainly Jurassic normal faults, and they follow the trends of the eastern and southwestern boundaries of the Polhem Subplatform; the north–south-trending Jason Fault complex; and the northwest–southeast-trending Ringvassøy-Loppa Fault complex.

Introduction

Unconformities and faults are considered key features in understanding the evolution of sedimentary basins. Unconformities are stratigraphic sequence boundaries that typically represent changes in a depositional environment due to an erosional event or nondepositional hiatus, whereas faults are discontinuities in the earth caused by brittle fracturing and displacement of rock volumes. Interpreting these features and building a geological model can be time consuming, and a variety of computational and computer-assisted interpretative methods have been developed to speed up the interpretive process. Some of the more interesting methods proposed include fully automated interpretation (e.g., Bahorich and Farmer, 1995; Wu and Hale, 2015, 2016; Huang et al., 2017).

Automatic identification of sequence boundaries and faults was introduced by Bahorich and Farmer (1995) with the coherence cube. The coherence cube is generated with an algorithm that obtains measurements of a multitrace relationship based on the similarity of neighboring seismic signals to identify and quantify discontinuities in seismic data. Today, the most commonly used coherence algorithms are based on crosscorrelation (Bahorich and Farmer, 1995), eigenstructure (Gerszten-korn and Marfurt, 1999; Chopra, 2002), and semblance (Marfurt et al., 1998; Hale, 2013). Qi et al. (2017) propose a seismic image skeletonization algorithm to sharpen locally planar features, such as faults and stratigraphic edges, and improve the quality of coherence attributes. Additionally, seismic geometric attributes, e.g., curvature (Roberts, 2001) and flexure (Di and Gao, 2016), have been suggested as alternatives to the coherence cube.

Since the introduction of the coherence cube (Bahorich and Farmer, 1995), proposed methods for automated detection of sequence boundaries have typically been based on the principles of traditional seismic sequence stratigraphy (e.g., Barnes, 2000; Hoek et al., 2010; Qayyum et al., 2017, 2018). Barnes (2000) and Hoek et al. (2010) exploit the characterization of seismic reflection patterns to generate attributes that highlight angular

[1]Kalkulo AS, Simula Research Laboratory, Fornebu, Norway. E-mail: aina@simula.no.
[2]University of New South Wales, Petroleum Engineering, Sydney, Australia. E-mail: stuart.clark@unsw.edu.au.
[3]Lundin Norway AS, Lysaker, Norway. E-mail: jan-erik.lie@lundin-norway.no.
[4]University of Oslo, Department of Geosciences, Oslo, Norway. E-mail: j.i.faleide@geo.uio.no.

unconformities, and Qayyum et al. (2017, 2018) discuss how one can use semiautomatic Wheeler diagrams to detect unconformities (Wheeler, 1958). Among the most recent work on automatic unconformity, detection is a method proposed by Wu and Hale (2015) that highlights angular and parallel unconformities from the calculated difference of two seismic normal structure fields and two structure-tensor fields.

Numerous methods on automated interpretation of faults have been proposed in the last decades, and "ant tracking," where virtual ants track discontinuities within a coherence cube, was among the first (Pedersen et al., 2002, 2003). Recently, Araya-Polo et al. (2017) propose a deep-learning system to map out a subsurface fault network for raw (synthetic) seismic recordings, where the need for seismic processing is bypassed. More generally, existing methods for automatic fault interpretation are based on the use of coherence data, and Hale's (2013) fault-likelihood attribute, generated with a semblance-based coherence algorithm is frequently used (such as that by Torabi et al., 2016; Wu and Hale, 2016; Huang et al., 2017; Lomask et al., 2017). Torabi et al. (2016) propose a way of extracting and digitizing manually selected fault-segment coordinates from filtered fault-likelihood time slices. Lomask et al. (2017) use the fault-likelihood attribute to better constrain fracture models between wells, and with this suggest a way to automatically track and extract faults. Huang et al. (2017) introduce the use of convolutional neural networks trained to learn fault characteristics and predict faults from extracted features in a fault-likelihood cube. Wu and Hale (2016) define fault samples based on measured fault likelihood, dip, and strike for each pixel in an input image, and then they use these fault samples to construct fault surfaces with a 3D sampling grid. They address the problem of intersecting faults as their sampling grid searches for neighboring samples and create new ones if they are missing in the directions best aligned with the local dip and strike.

In this paper, unconformities are semiautomatically identified on the assumption that the stratigraphic stacking pattern and the seismic amplitudes above and below an unconformity are significantly different. This assumption limits the method to detect only angular unconformities and nonconformities. Instead of generating new attributes to highlight the unconformities (as, e.g., Barnes, 2000; Wu and Hale, 2015; Qi et al., 2017), we use combined information from available data (original seismic reflection data and global 2D autotracked reflection data) to extract detected unconformities as individual binary 3D surfaces. For our fault extraction, we use a binary representation of fault-likelihood data (Hale, 2013). Whereas existing methods typically grow fault surfaces from defined fault samples (Torabi et al., 2016) or fault pixels (Wu and Hale, 2016), we assume that each fault surface can be represented as one binary 3D object. We separate intersecting objects with the use of morphological filter operations and by assigning the objects to different dip cubes prior to the actual fault extraction. Finally, objects that meet a set of user-defined filter criterions, related to fault size, are extracted from each of the dip cubes.

All of our extracted unconformities and faults are stored in separate 3D matrices (ASCII format), and they can easily be exported to different seismic software platforms. Here, we export them to a commercial software platform to demonstrate the use of our methods in a case study. With this work, we aim to show how unconformities and faults can be extracted from seismic data semiautomatically with relatively basic image processing tools and, further, to show how this can be used to aid, supplement, or even avoid manual seismic interpretation. Our focus is on the application of the methods, and we have applied them on industry-based data in a well-studied area; the Polhem Subplatform in the southwestern Barents Sea north of Norway (Figure 1). The Polhem Subplatform developed through several stages of rifting, inversion, and subsidence interrupted by erosional events, and it is today situated on the western margin of the Loppa High (Gabrielsen et al., 1990). The area has commercial interest because it contains the Alta, Gotha, and Filicudi discoveries by Lundin Norway AS and the Johan Castberg discovery by Statoil ASA, and its complex geology makes it suitable for evaluation of our methods.

Data

Lundin Norway AS has provided 3D seismic data and associated attribute data for this study. Seismic attributes are derivatives of the original seismic data and can be used to highlight specific features such as discontinuities (Bahorich and Farmer, 1995), thin beds (Roden et al., 2017), or direct hydrocarbon identifiers (Roden et al., 2015). The attribute data used in this paper include global 2D autotracked reflection data and fault-likelihood data. The global 2D autotracked reflection data, from here on referred to as tracked reflection data, represent coherent seismic reflective interfaces and are generated with a seedless algorithm proprietary to Lundin Norway AS. This algorithm is completely automatic, and it tracks all reflective events, peaks, and troughs, on all vertical slices (inlines or crosslines) in a seismic cube. The fault-likelihood data represent quantified discontinuities based on their tendency to disrupt seismic data and are generated with a semblance-based coherence algorithm developed by Hale (2013). The seismic data are acquired in the Barents Sea north of Norway and cover most of the Polhem Subplatform, with a lateral size of approximately 120 km² and a vertical depth of 3, 5 s.

Geological framework of the study area

The Polhem Subplatform sits on the western flank of the Loppa High in the southwestern Barents Sea on the Norwegian continental shelf (Figure 2). The western Barents Sea constitutes a 300 km wide rift zone, thought

to have been formed mainly in the mid-Carboniferous (Gudlaugsson et al., 1998).

A general northeastern structural trend in the southwest Barents Sea has long been explained by a fracture system in the basement rocks, thought to have been established during the Caledonian orogeny (Gabrielsen et al., 1990, 1993; Ritzmann and Faleide, 2007). This model proposes a fracture system that influenced the tectonic phases in post-Caledonian times, with new stress regimes adapting to the established trend and reactivating preexisting faults. However, a more recent publication based on aeromagnetic surveys indicates a dominant north-northwest/south-southeast orientation in the basement rocks (Gernigon and Brönner, 2012), and new deep regional seismic profiles acquired in 2016 makes it possible to interpret deep features and therefore address the implications of Caledonian thrust tectonics (Lie et al., 2017).

In the southwestern part of the Barents Sea, the subsurface consists of Caledonian metamorphic basement rocks covered by sedimentary packages ranging in ages from the Late Paleozoic to the present (Breivik et al., 1998; Ritzmann and Faleide, 2007; Glørstad-Clark et al., 2010). The area has experienced a complex history of crustal thinning, with four assumed main rift phases; in Mid Carboniferous, Late Permian, Late Jurassic to Early Cretaceous, and in Late Cretaceous-Paleocene. The phases of extension have contributed to a series of rifting, subsidence, tilting, uplift, erosion, and inversion events, and they have led to the formation of basins and highs in the Barents Sea, such as the Loppa High (Gabrielsen et al., 1990, 1993; Gudlaugsson et al., 1998).

The Loppa High was a sedimentary depocenter in the Triassic to Jurassic that was uplifted during early Cretaceous rifting and became subaerially exposed and subjected to erosion (Wood et al., 1989; Faleide et al., 1993; Glørstad-Clark et al., 2010). A recent study on inversion structures in the southwest Barents Sea by Indrevær et al. (2016) suggests that the initiation of uplift of the Loppa High can be dated to Barremian time. As a consequence of the Early Cretaceous uplift, Jurassic and Cretaceous sedimentary beds are eroded and thin to not present on the Loppa High, whereas they thicken into the deeper basins surrounding it. The Cenozoic strata on Loppa include a thin layer of Neogene glacial sediments, whereas Paleogene strata only can be found in the basins surrounding the high (Fiedler and Faleide, 1996).
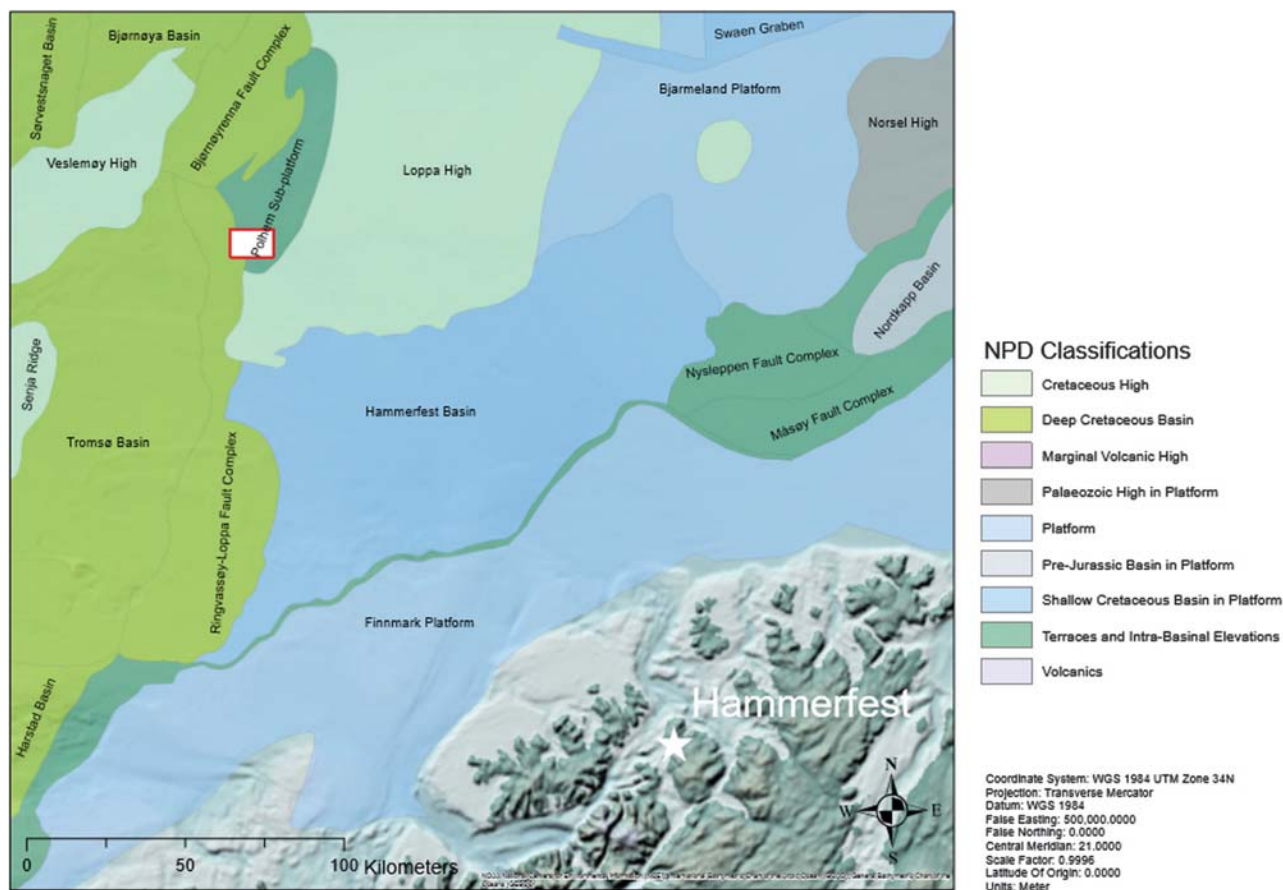
Figure 1. Map of the regional structures in the southwestern Barents Sea, north of Norway. The study area is annotated with a red square and covers parts of the Polhem Subplatform at the left flank of the Loppa High. The map includes topography by NOAA and geological classification by NPD, as well as Norway's northern coastline and the city of Hammerfest.

The Polhem Subplatform is separated from Loppa by the Jason Fault complex, which defines the western flank of the Selis ridge, a Late Paleozoic structure (Glørstad-Clark et al., 2011a). Southwest of Polhem, the Ringvassøy-Loppa Faults complex defines the transition into the Tromsø Basin (Gabrielsen et al., 1990). The major faults on the Polhem Subplatform are in general extensional faults of Jurassic to Early Cretaceous age (Gabrielsen et al., 1993).

Semiautomatic seismic feature extraction

We present two independent methods for semiautomatic extraction of unconformities and faults from seismic data in this paper. As stated in the "Introduction" section, automatic detection and extraction of unconformities and faults usually require different approaches, with Bahorich and Farmer's (1995) coherence cube being an exception. Both methods use commonly known image processing functions such as morphological operations and filter operations for image region properties, and all processing has been executed in MATLAB with use of the Image Processing Toolbox. Prior to processing, the seismic volumes are converted from SEG-Y format to matrices with the segyMAT library (Thomas, 2001). Our methods rely on 2D and 3D operations, where the 2D operations are used on inlines, crosslines, and/or time slices, and the 3D operations are used on seismic volumes.

Unconformity extraction

Unconformities represent time gaps, and they can usually be recognized by dating or by using Hutton's principle. Here, we semiautomatically detect and extract unconformities from seismic data based on the assumption that they separate sequences of significantly different stacking patterns and brightness in the seismic amplitudes. Unconformities that do not separate significantly different sequences, such as paraunconformities or disconformities, will not be detected with this method.

To define different stacking patterns, each reflection (in the tracked reflection data) is treated as one binary object with a measured orientation and with measured distances to its neighbor objects. The orientation is measured on 2D seismic lines as the angle between the main axis of the reflection and the x-axis of the seismic line. Distances are measured as the smallest distance between two reflections on a seismic line in number of pixels. Reflections with similar orientation and within a close distance to each other are grouped and assigned to the same stacking pattern (Figure 3). This process is semiautomatic because the user defines how large the distance between reflections in the same pattern can be and the range of orientations for each pattern. Thus, the user controls the number of stacking patterns, and prior knowledge of the sequence stratigraphy in the given area is helpful, but not required as the computational efficiency of the method allows the user to test and reset parameters for optimal results.
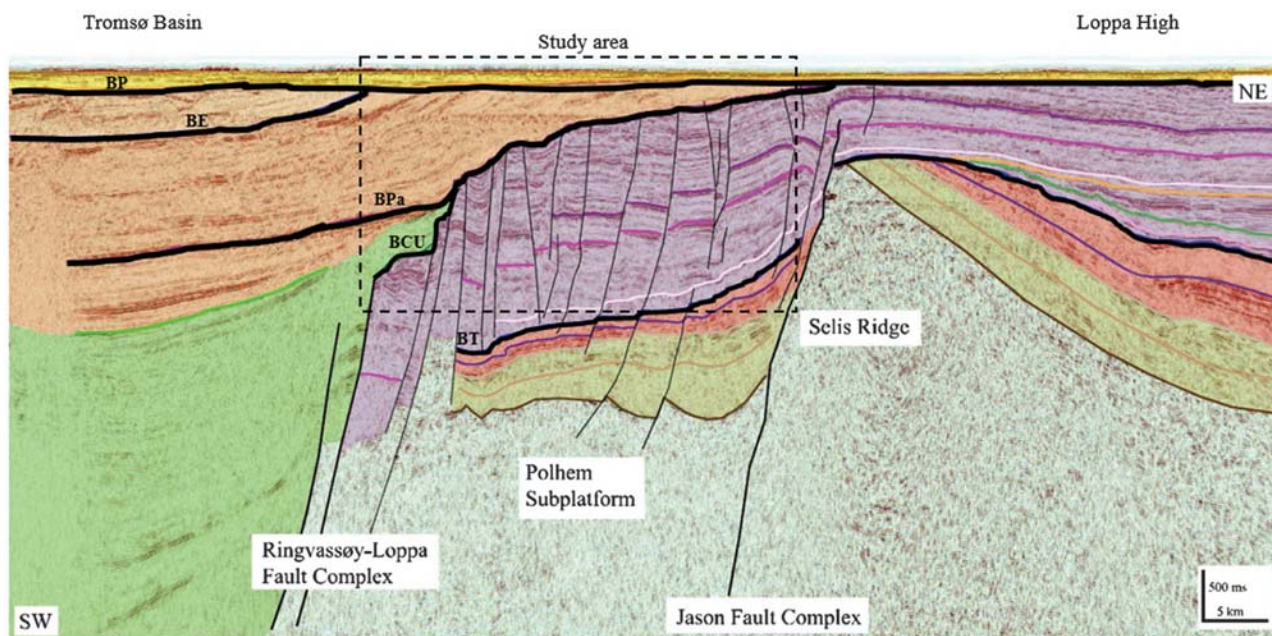
Figure 2. A manually interpreted seismic line of the Polhem Subplatform with the Loppa High to the northeast and the Tromsø Basin to the southwest. The figure is modified from Glørstad-Clark et al. (2011b). Megasequences are given distinct colors, and some important sequence boundaries are annotated: BP, Base Pleistocene; BE, Base Eocene; BT, Base Triassic; BPa, Base Paleocene; and BCU, Base Cretaceous Unconformity. The Base Paleocene and the Base Cretaceous merge together on Polhem and Loppa. The Ringvassøy-Loppa Fault Complex and the Jason Fault Complex are the boundary faults of the Polhem Subplatform.

To detect changes in the seismic amplitudes, we have applied a Sobel edge-detection algorithm on the original seismic data. Edge detection is an intensity-based image analysis that computes an approximation of the gradient of the image intensity function, and it is generally used to find sharp changes in brightness in digital images. When applied to seismic data, the edge detection highlights edges between reflections that show significant amplitude differences, and (more importantly for us) indicate transitions between high- and low-intensity regions in the seismic data (Figure 4).

Each stratigraphic stacking pattern is combined with the edge-detection data to define one seismic sequence. One sequence will thus have a stacking pattern and seismic amplitudes that in general differ from those of the sequences surrounding it. Further, its top or base boundary is extracted and stored in a binary 3D matrix, assumed to represent one unconformity (Figure 5). The method involves 2D processing of 3D data and is applied in the inline and crossline directions. For robust results, only intersecting results from the inline and crossline processings should be kept.

Fault extraction

With our method for semiautomatic fault extraction, we assume that each fault surface can be targeted as a 3D object in a binary representation of the fault-likelihood cube (Hale, 2013). Prior to this, we address interference within the cube by separating intersecting faults through binary image operations. See Bugge (2016) for a discussion on the use of binary operations to filter coherence data.

The separation of intersecting faults involves a series of 2D processing steps, where the first step is to use morphological operations to remove branch points within the cube. A branch point is defined as where a pixel is connected to three-or-more neighboring pixels, and the operation requires a skeletonized input image (infinitely thinned faults). This process removes too much information when applied on inlines and crosslines, and it is thus applied only on time slices here. Our finally extracted faults will thus be slightly thinned compared with their original shape in the fault-likelihood cube. Because the branch points are removed
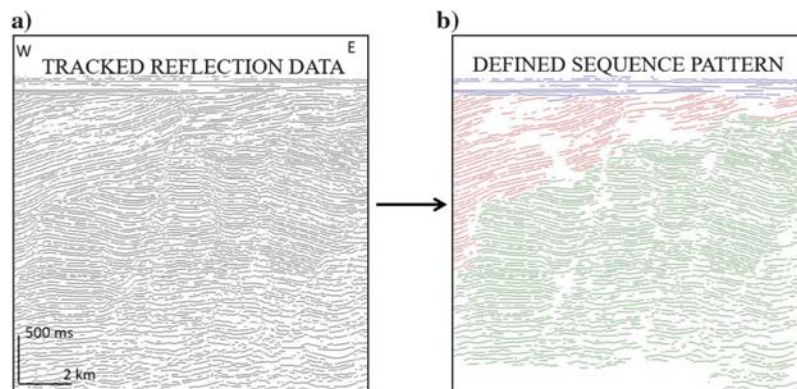
Figure 3. (a) Two-dimensional seismic lines of the tracked reflection data and (b) the semiautomatically defined stratigraphic stacking patterns. The stacking patterns are defined based on the orientation of each reflection and the distances between them. Each pattern is given a distinct color: blue, red, or green.
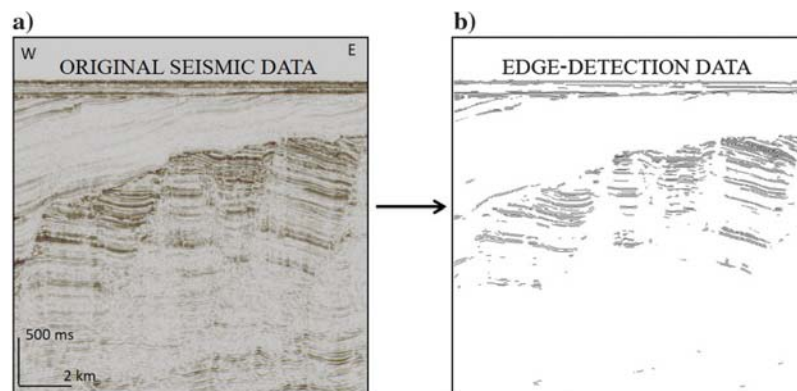
Figure 4. (a) Two-dimensional seismic lines of the original seismic data and (b) adjacent edge-detection data. The edge-detection data are generated with a Sobel edge-detection algorithm applied on the original seismic data and indicate changes in the seismic amplitudes.
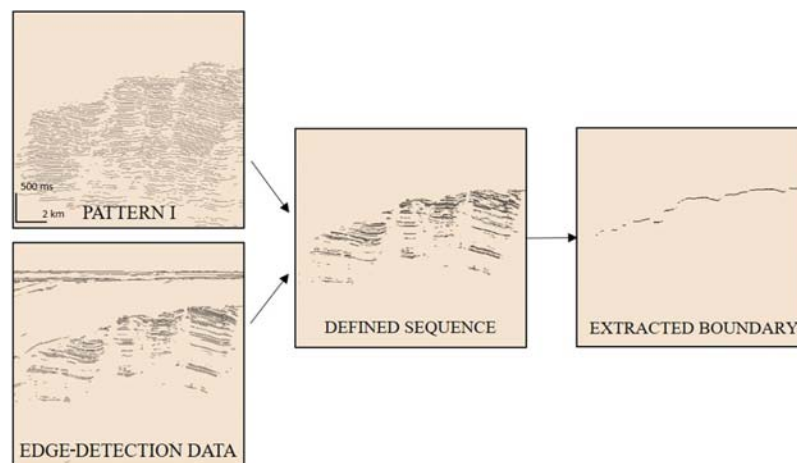
Figure 5. Our method on semiautomatic extraction of one unconformity illustrated step-by-step on one 2D line. First, one defined stratigraphic stacking pattern is combined with the edge-detection data to create a seismic sequence, and then all top pixels in the sequence are extracted to give the top boundary. This boundary is the assumed unconformity.

solely on time slices, further separation of interfering objects is necessary. We address this by assigning objects to new empty dip cubes based on their apparent dip in 2D. This dip is defined as the measured 2D orientation (in degrees) of the main axis of each object on a seismic line in relation to the x-axis of the line. When this is done for all seismic lines in the fault cube, the new dip cubes will consist of 3D objects with little to no interference because all objects dip in a similar direction. We chose to use two dip cubes here because this sufficiently separates intersecting faults and because choosing too many dip cubes tends to cause major listric faults to break with depth.

Further, each dip cube is processed individually. From each cube, objects that pass a set of user-defined criterions are extracted and assumed to represent individual fault surfaces. The criterions are related to 3D measurements of the volumetric size and longest length of each object, where size is measured in the number of connected pixels and length is measured as the length of the object's principal axis, also in the number of pixels. The main steps of the fault-extraction method are illustrated in Figure 6.

Our method for fault extraction is time efficient and relatively comprehensible, and the user can change filter criterions to adapt the method and optimize the result for different input data and use. The method does not rely on the initial fault-likelihood values, only a binary representation of them, and it is likely that we could have used other, less computationally expensive, fault attributes than the fault likelihood.

Results

In our case study, we use the presented methods for feature extraction to semiautomatically interpret unconformities and faults on the Polhem Subplatform. This outputs three surfaces (S1–S3) and 25 faults (F1–F25). Each extracted feature is a 3D binary object that can be exported to different software platforms for visualization and for various uses. Figure 7 shows cross sections of the surfaces and faults on a seismic line, and in Figure 8, all three surfaces and the three largest faults are exported to Petrel E&P Software Platform and visualized in 3D from different views. No smoothing or filling of holes has been done here, but such tools (manual and/or automatic) are available in most seismic interpretive software.

The three extracted surfaces, S1–S3, all represent significant changes in stratigraphic stacking patterns and in seismic amplitudes. However, only the latter two are assumed to be unconformities because S1 represents the seabed. S2 is a near-horizontal and continuous surface, where the over- and underlying sequences have consistent and significantly different seismic character within the study area. This surface is assumed to represent the Base Pleistocene, which was developed in the Late Neogene when glaciers eroded the Norwegian shelf, and it separates glacially derived Pliocene to Pleistocene sediments from underlying preglacial Paleocene sediments deposited during the time the Atlantic Ocean opened between Norway and Greenland (Fiedler and Faleide, 1996; Dimakis et al., 1998). The glaciers are believed to have eroded 500–1000 m in the area around the Loppa High, and consequently, Paleocene sediments are not present on the high itself (Wood et al., 1989). They can, however, be found on the Polhem Subplatform and in the basins surrounding it, such as in the Tromsø Basin, where they have A westward dip and an increasing thickness into the center of the basin (Henriksen et al., 2011).

S3 is less continuous and is thought to be the base Cretaceous unconformity (BCU); the unconformable sequence boundary that separates Paleocene sediments from underlying pre-Cretaceous, Mesozoic sediments in the study area. This unconformity is associated with several phases of uplift and erosion and is in many places a composite unconformity of the BCU and the Base Paleocene unconformity. The Base Paleocene intersects the BCU on the transition to the Polhem Subplatform from the Tromsø Basin (Figure 7) and the extraction of S3 is inconsistent near this transition. The Mesozoic strata below the BCU are mainly of Triassic age and
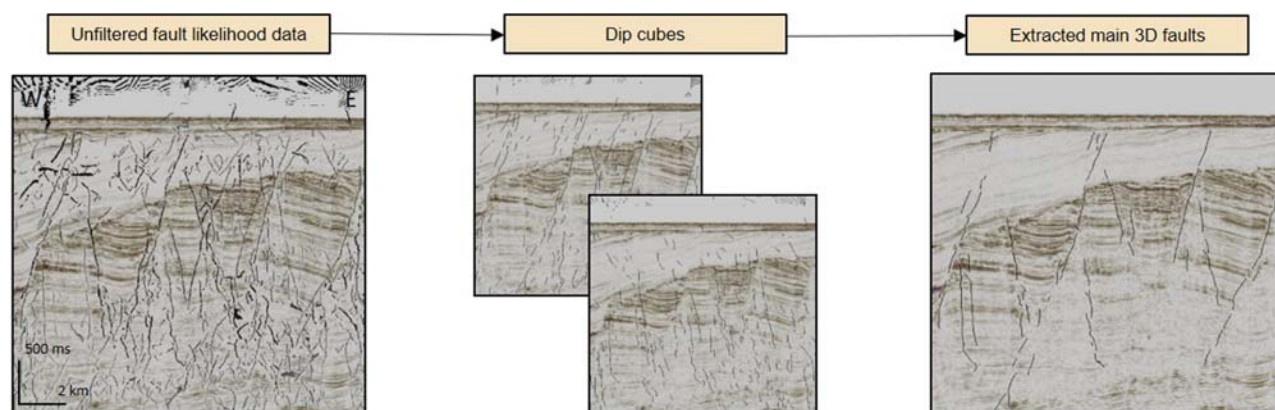
Figure 6. Step-by-step illustration of the semiautomatic fault extraction on one 2D line. Fault-likelihood data are first subjected to morphological filter operations before objects are assigned to different dip cubes. Further, the major faults are extracted from each of the dip cubes, based on 3D user-defined criterion.

are the results of a strong sedimentary influx, which led to thick accumulation of west to northwest prograding deltaic wedges (Glørstad-Clark et al., 2011a). Subsequent tectonic activity caused the Mesozoic strata to experience massive normal faulting and fault block rotation, and they generally have a downward dip to the east. Due to this tectonic activity, the Mesozoic stacking pattern shows significant lateral differences and S3 has gaps of missing data in the most heavily faulted areas. Even though Jurassic bedrock is almost nonexistent on the Loppa High, there are (assumed) local deposits of sand wedges of Late Jurassic to Early Cretaceous age in the study area (Figure 7). These are thought to be erosional products from the time when Loppa was uplifted (Indrevær et al., 2016), and they cause inconsistent extraction of S3 because their characteristics do not match their over- or underlying (Paleogene or Mesozoic) seismic sequence.

The 25 extracted faults are assumed to be Mesozoic faults because they are in general normal faults that separate fault blocks in the Mesozoic strata, below the BCU. Some of the main faults (e.g., F1 and F2) cut through the Mesozoic and the overlying Paleogene successions and indicate activity in more than one tectonic event, presumably in the Late Jurassic to Early Cretaceous and in the (less prominent) Late Cretaceous to Paleocene rift phase. The faults follow the trends of the Polhem Subplatform boundary faults; the north–south-trending Jason Fault complex in the east, and the northwest–southeast-trending Ringvassøy-Loppa Fault complex in the west (Glørstad-Clark et al., 2011a; Serck et al., 2017). The north–south trend is believed to

have been formed in the Permian, it reactivated later in the Mesozoic, and it continues north of the Polhem Subplatform along the eastern boundary fault of the Bjørnøya Basin and the western boundary fault of the Fingerdjupet Basin (Serck et al., 2017).

The fault extraction is generally successful in extracting the dominating faults in the study area and in separating intersecting faults. However, the method fails to separate similarly dipping faults that merge into the same fault plane, as is the case for F2. In Figure 7, F2a and F2b appear as two objects, whereas the 3D view in Figure 8 shows how they merge together. Separating such faults and/or applying smoothing must be done carefully (if at all). Faults seldom act as individual fault planes, but rather as fault segments in fracture zones, and attempts to single out segments from these zones before the application of filter operations could lead to loss of information (at least with our method). Because no smoothing or filling of holes have been done here, faults that are connected in 3D may appear as broken on 2D cross sections (Figure 7). Also, where the data quality is poor, the faults tend to break. This is a common issue with automatic fault detection and is here best observed with F7 in Figure 7.

Discussion

It takes less than 10 min to extract the 3D unconformities and faults in the study area (see the recorded processing times in Table 1). For the processing, we have used an Intel Core i7-6500U CPU processor, and our input data have 169,419,276 data points. Note that
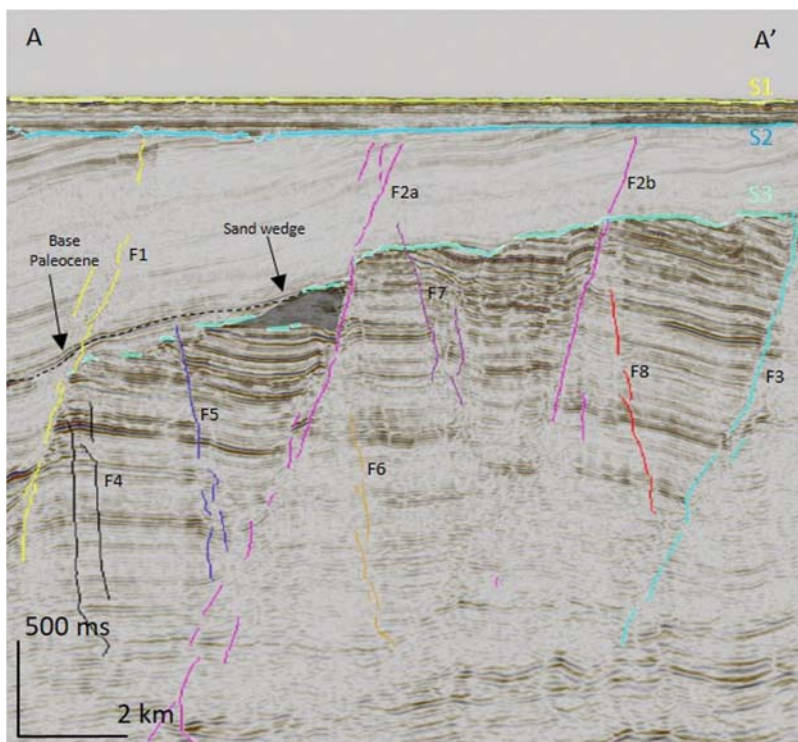
Figure 7. A 2D seismic line of the Polhem Subplatform with superimposed cross sections of 3D semiautomatically extracted unconformities (S1–S3) and faults (F1–F8). As the figure shows 2D cross sections of 3D objects, the apparent continuity of them can be delusive. Each object has a distinct color indicating that it is connected in 3D.

this is not including the time it takes to generate the attribute data. Both methods are considered semiautomatic because they rely on some user interaction. The unconformity extraction is based on user-defined criterions to define the stratigraphic stacking patterns. As the tracked reflection attribute is generated with a 2D algorithm, we can only measure reflector orientation and define stacking patterns in 2D. This is consid-ered a limitation with the method, and a potential improvement would be to instead use true 3D orientation in space (magnitude and direction). The fault extraction is near completely automatic because the only required user interaction is the definition of the filter criterions — the minimum size and length of the extracted faults. No geological knowledge is necassary as the criterions can be decided by testing, depending on the wanted number of extracted faults. As discussed in the "Introduction" section, many methods for automatic fault extraction already exist, but our method benefits from being time-efficient, relatively comprehensible, and requiring only easily available tools.

To test the generic use of our methods, we have applied them on new data outside of the main study area. These results are displayed in Figure 9. The unconformity extraction is applied on a 2D seismic line covering approximately 56 km laterally, where five 2D boundaries are identified and extracted. Because these new input data are a 2D seismic line, the results are less robust than the results obtained with the 3D data presented in the case study. Also, because this seismic line covers a larger area laterally, there are more variations within each stacking pattern and the method fails to detect the full extent of some of the extracted unconformities. This could potentially be avoided by processing on smaller overlapping sub-slices (or subcubes in 3D). The fault extraction is applied on a new 3D fault-likelihood cube, approximately six times larger than the one used in the case study. We successfully extract the largest faults within this cube, with no additional remarks beyond what was observed in the case study.

A detailed analysis of the stratigraphic stacking patterns beneath the BCU reveal that the Mesozoic fault blocks, in addition to having the general eastern dip explained in the "Results" section, also dip either north or south in an alternating sequence (Figure 10). A few of the fault blocks even indicate a concave/convex dip. These dipping fault blocks fit well together with the extracted normal faults, and the characterization of the relationship between the Mesozoic fault blocks can be used to better understand the development of the Loppa High and the Polhem Subplatform. Additionally, knowledge of how the fault blocks are tilted and rotated with respect to each other could be used to aid seismic reconstruction in time and space. The process of recon-
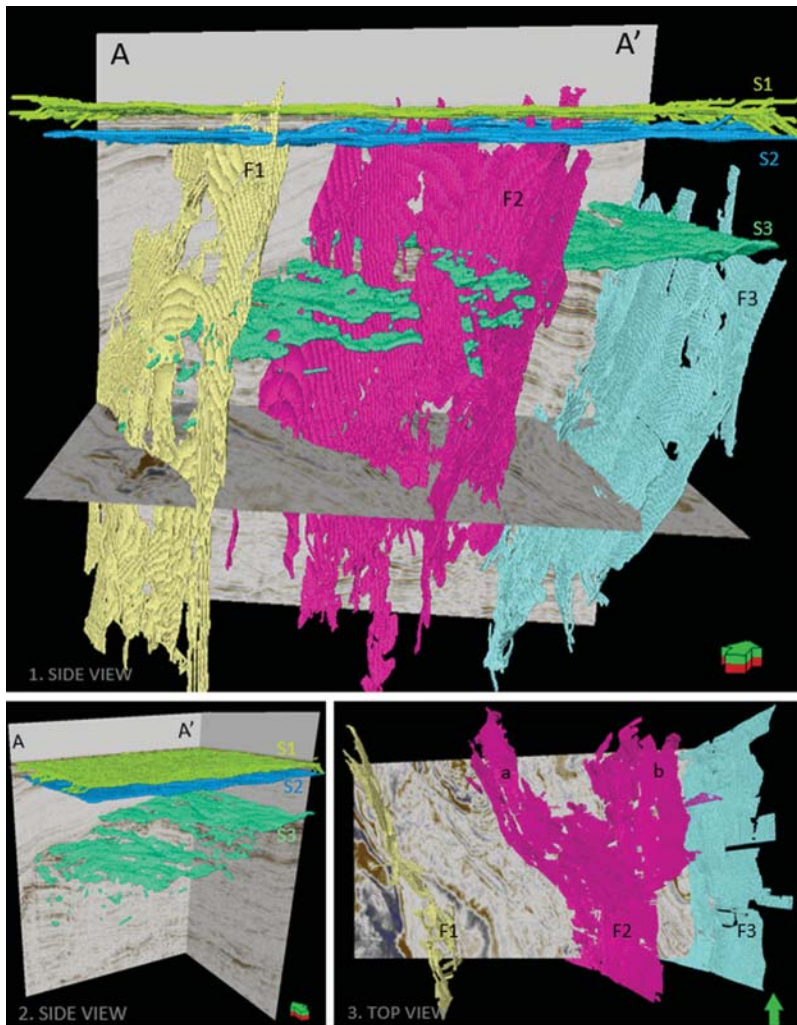

Figure 8. Three-dimensional visualization of the semiautomatically the extracted unconformities (S1–S3) and of three selected major faults (F1–F3), here exported to Petrel E&P Software as ASCII-files (IRAP points). The green arrow indicates the way up and points north. Each 3D object has its own color.

Table 1. Processing times for 3D semiautomatic feature extraction on the Polhem Subplatform.

	Unconformity extraction	Fault extraction
Processing time	559.4 s	557.9 s
Output	3 surfaces	25 faults
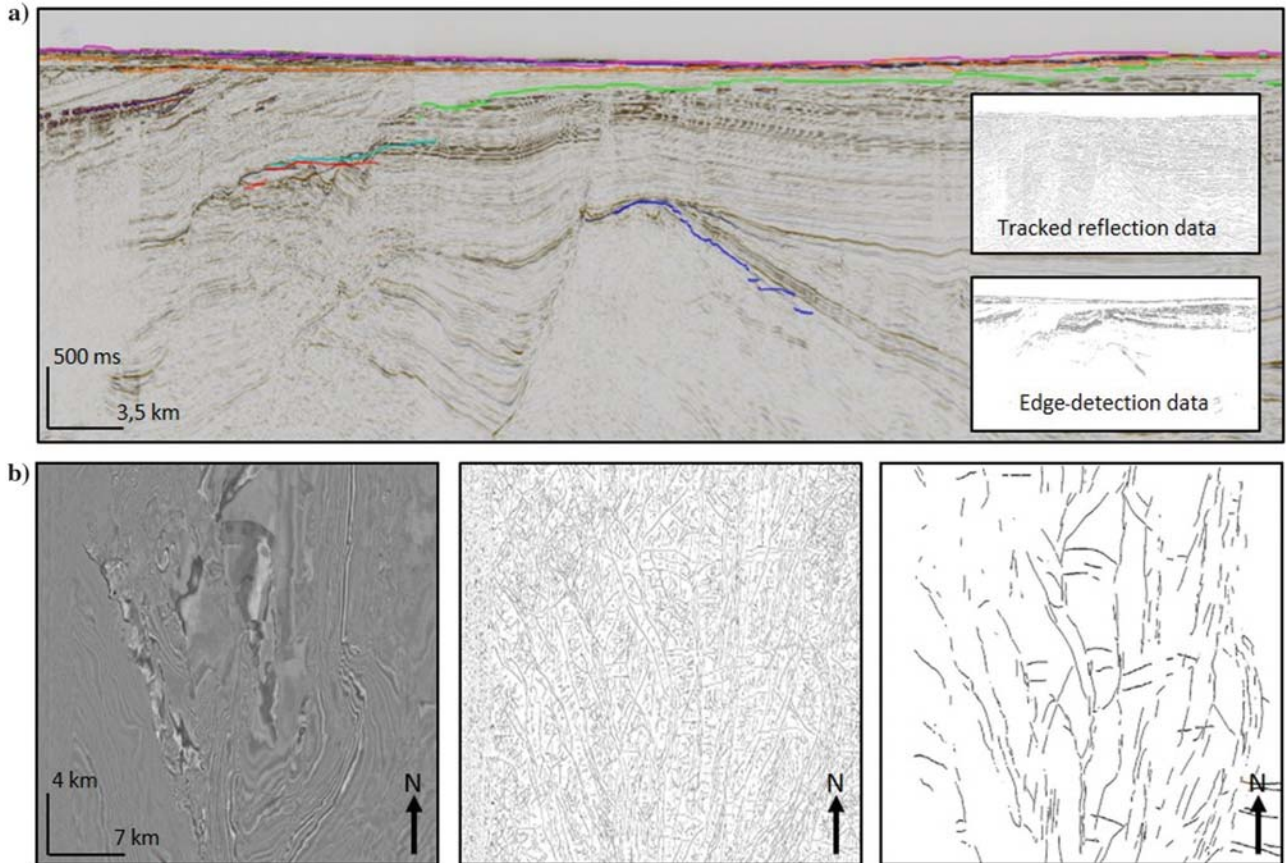
Figure 9. The two presented methods are applied on data outside our main study area. (a) This results in six semiautomatically interpreted boundaries, extracted from a 2D line covering approximately 56 km laterally, and (b) semiautomatic extraction of major faults in a fault-likelihood volume approximately six times the size of our study area. The faults are here displayed on a time slice, and they are slightly thickened for better visualization. For comparison, a binary unfiltered time slice from the same fault-likelihood volume is included.
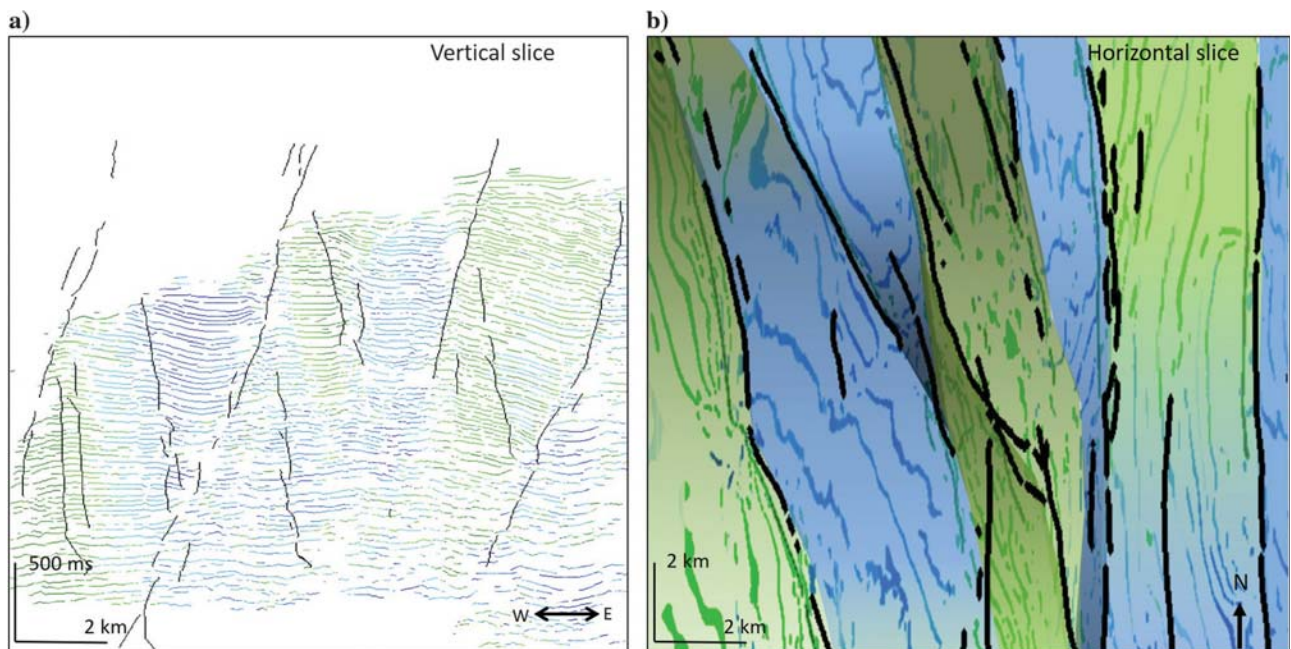
Figure 10. (a) A seismic line and (b) a seismic time slice from the tracked reflection data, where the color indicates the dip of the reflections. Semiautomatically extracted faults are superimposed to the tracked reflection data. This reveals an alternating northern (green) and southern (blue) dip of the Mesozoic fault blocks. Faded colors indicate a concave/convex dip.
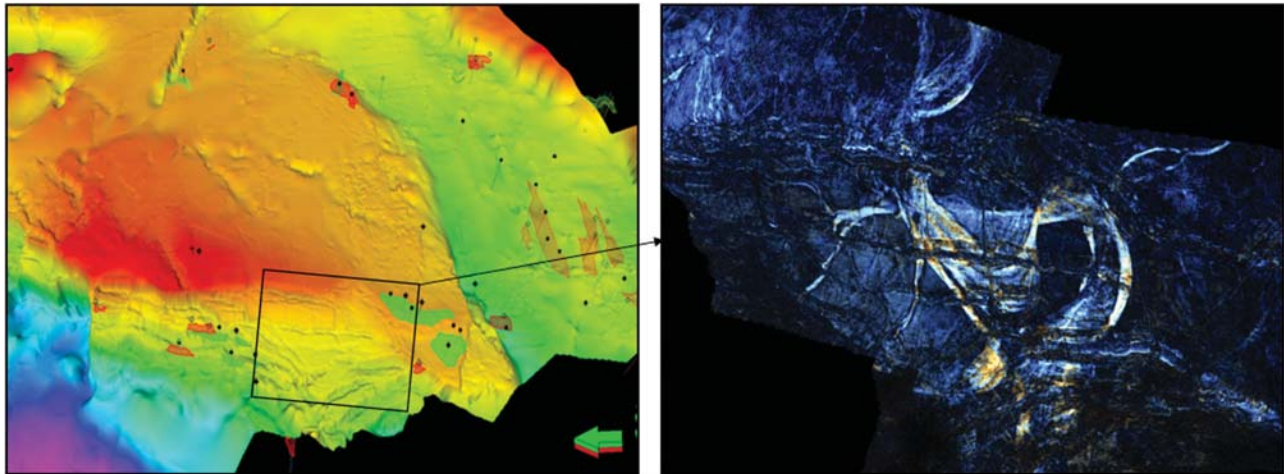
Figure 11. Automated seismic reconstruction in time and space is one of the motivations behind this work. Reconstructed seismic data make it possible to instantly pick horizon slices (which can be used in, e.g., a search for geobodies), as illustrated with this figure. Here, amplitude extraction from top Snadd horizon slice (Late Middle-Early Late Triassic) reveals a massive paleochannel system in the Loppa High area. Data are provided by Lundin Norway AS.

structing seismic data is time consuming and difficult, especially step wise, and a lot could be gained from automating the process. Structural and temporal seismic reconstructions are important for understanding the earth's subsurface and its evolution and make it possible to instantly pick horizon slices without the need for manual interpretation. This could, for example, aid the search for geobodies, such as paleochannels, which are usually best detected and interpreted on horizon slices (see Figure 11).

Conclusion

In this paper, we have presented methods for semiautomatic seismic interpretation through the extraction of 3D unconformities and faults. The two methods are independent, and they are based on existing 2D and 3D image processing algorithms. Both methods are time-efficient and are considered as useful tools in seismic interpretive studies because they can be used to aid, reduce, or avoid traditional manual seismic interpretation. In this study, we have implemented the proposed methods with a case study on the Polhem Subplatform in the Barents Sea, a geologically complex area, which has experienced a series of rifting, subsidence, tilting, uplift, erosion, and inversion events. In the study area, the methods extract two unconformities; the Base Pleistocene and the Base Cretaceous, and 25 faults; large Jurassic normal faults with north–south or northwest–southeast structural trends.

Acknowledgments

References

Araya-Polo, M., T. Dahlke, C. Frogner, T. Poggio, and D. Hohl, 2017, Automated fault detection without seismic processing: The Leading Edge, **36**, 208–214, doi: 10.1190/tle36030208.1.

Bahorich, M., and S. Farmer, 1995, 3-D seismic discontinuity for faults and stratigraphic features: The coherence cube: The Leading Edge, **14**, 1053–1058, doi: 10.1190/1.1437077.

Barnes, A. E., 2000, Attributes for automating seismic facies analysis: 70th Annual International Meeting, SEG, Expanded Abstracts, 553–556.

Breivik, A. J., J. I. Faleide, and S. T. Gudlaugson, 1998, Southwestern Barents Sea margin: Late Mesozoic sedimentary basins and crustal extension: Tectonophysics, **293**, 21–44, doi: 10.1016/S0040-1951(98)00073-0.

Bugge, A. J., 2016, Binary filters developed to enhance and extract features and trends from 3D fault likelihood coherence data: M.S. thesis, University of Oslo.

Chopra, S., 2002, Coherence cube and beyond: First Break, **27**, 20–33, doi: 10.1046/j.1365-2397.2002.00225.x.

Di, H., and D. Gao, 2016, Improved estimates of seismic curvature and flexure based on 3D surface rotation in the presence of structure dip: Geophysics, **81**, no. 2, IM13–IM23, doi: 10.1190/geo2015-0258.1.

Dimakis, P., B. I. Braathen, J. I. Faleide, A. Elverhøi, and S. T. Gudlaugsson, 1998, Cenozoic erosion and the preglacial uplift of the Svalbard-Barents Sea region: Tectonophysics, **300**, 311–327, doi: 10.1016/S0040-1951(98)00245-5.

Faleide, J. I., E. Vagnes, and S. T. Gudlaugson, 1993, Late Mesozoic-Cenozoic evolution of the south-western Barents Sea in a regional rift-shear tectonic setting: Marine and Petroleum Geology, **10**, 186–214, doi: 10.1016/0264-8172(93)90104-Z.

Fiedler, A., and J. I. Faleide, 1996, Cenozoic sedimentation along the southwestern Barents Sea margin in relation

to uplift and erosion of the shelf: Global and Planetary Change, **12**, 75–93, doi: 10.1016/0921-8181 (95)00013-5.

Gabrielsen, R. H., R. Færseth, L. N. Jensen, J. E. Kalheim, and F. Riis, 1990, Structural elements of the NCS. Part I: The Barents Sea Region: NPD–Bulletin, 1–33.

Gabrielsen, R. H., I. Grunnaleite, and S. Ottesen, 1993, Reactivation of fault complexes in the Loppa High area, southwestern Barents Sea: Norwegian Petroleum Society Special Publications, **2**, 631–641, doi: 10.1016/B978-0-444-88943-0.50041-1.

Gernigon, L., and M. Brönner, 2012, Late Palaeozoic architecture and evolution of the southwestern Barents Sea: Insights from a new generation of aeromagnetic data: Journal of the Geological Society, **169**, 449–459, doi: 10.1144/0016-76492011-131.

Gersztenkorn, A., and K. J. Marfurt, 1999, Eigenstructure-based coherence computations as an aid to 3-D structural and stratigraphic mapping: Geophysics, **64**, 1468–1479, doi: 10.1190/1.1444651.

Glørstad-Clark, E., E. P. Birkeland, J. P. Nystuen, J. I. Faleide, and I. Midtkandal, 2011a, Triassic platform-margin deltas in the western Barents Sea: Marine and Petroleum Geology, **28**, 1294–1314, doi: 10.1016/j.marpetgeo.2011.03.006.

Glørstad-Clark, E., S. A. Clark, J. I. Faleide, S. S. Bjørkesett, R. H. Gabrielsen, and J. P. Nystuen, 2011b, Basin dynamics of the Loppa High area, SW Barents Sea: A history of complex vertical movements in an epicontinental basin, in E. Glørstad-Clark, ed., Basin analysis in the western Barents Sea area: The interplay between accommodation space and depositional systems: University of Oslo.

Glørstad-Clark, E., J. I. Faleide, B. A. Lundschien, and J. P. Nystuen, 2010, Triassic seismic sequence stratigraphy and paleogeography of the western Barents Sea area: Marine and Petroleum Geology, **27**, 1448–1475, doi: 10.1016/j.marpetgeo.2010.02.008.

Gudlaugsson, S. T., J. I. Faleide, S. E. Johansen, and A. J. Breivik, 1998, Late Palaeozoic structural development of the South-western Barents Sea: Marine and Petroleum Geology, **15**, 73–102, doi: 10.1016/S0264-8172 (97)00048-2.

Hale, D., 2013, Methods to compute fault images, extract fault surfaces, and estimate fault throws from 3D seismic images: Geophysics, **78**, no. 2, O33–O43, doi: 10.1190/geo2012-0331.1.

Henriksen, E., A. E. Ryseth, G. B. Larsen, T. Heide, K. Rønning, K. Sollid, and A. V. Stoupakova, 2011, Chapter 10: Tectonostratigraphy of the greater Barents Sea: Implications for petroleum systems: Geological Society Memoir, **35**, 163–195, doi: 10.1144/M35.10.

Hoek, T., S. Gesbert, and J. Pickens, 2010, Geometric attributes for seismic stratigraphic interpretation: The Leading Edge, **29**, 1056–1065, doi: 10.1190/1.3485766.

Huang, L., X. Dong, and T. E. Clee, 2017, A scalable deep learning platform for identifying geologic features from seismic attributes: The Leading Edge, **36**, 249–256, doi: 10.1190/tle36030249.1.

Indrevær, K., R. H. Gabrielsen, and J. I. Faleide, 2016, Early Cretaceous synrift uplift and tectonic inversion in the Loppa High area, southwestern Barents Sea, Norwegian shelf: Journal of the Geological Society, 242–254, doi: 10.1144/jgs2016-066.

Lie, J. E., M. Anderson, and S. Clark, 2017, New regional deep seismic profiles: Imaging the crust of the Norwegian Barents Sea: Program Arctic Energy — Arctic Days 2017, Norsk Geologisk Forening.

Lomask, J., L. Hernandez, V. Liceras, A. Kumar, and A. Khadeeva, 2017, A seismic to simulation unconventional workflow using automated fault-detection attributes: Interpretation, **5**, no. 3, SJ41–SJ48, doi: 10.1190/INT-2016-0148.1.

Marfurt, K. J., R. L Kirlin, S. L. Farmer, and M. S. Bahorich, 1998, 3-D seismic attributes using a semblance-based coherency algorithm: Geophysics, **63**, 1150–1165, doi: 10.1190/1.1444415.

Pedersen, S. I., T. Randen, L. Sønneland, and Ø. Steen, 2002, Automatic fault extraction using artificial ants: 72nd Annual International Meeting, SEG, Expanded Abstracts, 512–515.

Pedersen, S. I., T. Skov, A. Hetlelid, P. Fayemendy, T. Randen, and L. Sønneland, 2003, New paradigm of fault interpretation: 73rd Annual International Meeting, SEG, Expanded Abstracts, 350–353.

Qayyum, F., C. Betzler, and O. Catuneanu, 2017, The wheeler diagram, flattening theory, and time: Marine and Petroleum Geology, **86**, 1417–1430, doi: 10.1016/j.marpetgeo.2017.07.034.

Qayyum, F., C. Betzler, and O. Catuneanu, 2018, Space-time continuum in seismic stratigraphy: Principles and norms: Interpretation, **6**, no. 1, T97–T108, doi: 10.1190/INT-2017-0061.1.

Qi, J., G. Machado, and K. J. Marfurt, 2017, A workflow to skeletonize faults and stratigraphic features: Geophysics, **82**, no. 4, O57–O70, doi: 10.1190/geo2016-0641.1.

Ritzmann, O., and J. I. Faleide, 2007, Caledonian basement of the western Barents Sea: Tectonics, **26**, 1–120.

Roberts, A., 2001, Curvature attributes and their application to 3D interpreted horizons: First Break, **19**, 85–100, doi: 10.1046/j.0263-5046.2001.00142.x.

Roden, R., T. Smith, and D. Sacrey, 2015, Geologic pattern recognition from seismic attributes: Principal component analysis and self-organizing maps: Interpretation, **3**, no. 4, SAE59–SAE83, doi: 10.1190/INT-2015-0037.1.

Roden, R., T. Smith, P. Santogrossi, D. Sacrey, and G. Jones, 2017, Seismic interpretation below tuning with multi-attribute analysis: The Leading Edge, **36**, 330–339, doi: 10.1190/tle36040330.1.

Serck, C. S., J. I Faleide, A. Braathen, B. Kjølhamar, and A. Escalona, 2017, Jurassic to early cretaceous basin configuration(s) in the Fingerdjupet Subbasin, SW Barents

Sea: Marine and Petroleum Geology, **86**, 874–891, doi: 10.1016/j.marpetgeo.2017.06.044.

Thomas, M. H., 2001, SegyMAT : Read and Write SEG-Y files using Matlab and Octave, http://segymat.sourceforge.net/, accessed 3 March 2018.

Torabi, A., B. Alaei, D. Kolyukhin, A. Libak, R. H. Gabrielsen, and A. Braathen, 2016, Fault geometric and seismic attributes: An integrated study with focus on the Barents Sea: First Break, **34**, 51–58.

Wheeler, H. E., 1958, Time-stratigraphy: Bulletin of the American Association of Petroleum Geologists, **42**, 1047–1063.

Wood, R. J., S. P. Edrich, and I. Hutchison, 1989, Influence of North Atlantic tectonics on the large-scale uplift of the Stappen High and Loppa High, western Barents Shelf, in A. J. Tankard and H. R. Balkwill, eds., Extensional tectonics and stratigraphy of the North Atlantic Margins: AAPG Memoirs, 559–566.

Wu, X., and D. Hale, 2015, 3D seismic image processing for unconformities: Geophysics, **80**, no. 2, IM35–IM44, doi: 10.1190/geo2014-0323.1.

Wu, X., and D. Hale, 2016, 3D seismic image processing for faults: Geophysics, **81**, no. 2, IM1–IM11, doi: 10.1190/geo2015-0380.1.

Biographies and photographs of the authors are not available.

II

Automatic extraction of dislocated horizons from 3D seismic data using nonlocal trace matching

Aina Juell Bugge[1], Jan Erik Lie[2], Andreas Kjelsrud Evensen[2], Jan Inge Faleide[3], and Stuart Clark[4]

ABSTRACT

Extracting key horizons from seismic images is an important element of the seismic interpretation workflow. Although numerous computer-assisted horizon extraction methods exist, they are typically sensitive to structural and stratigraphic discontinuities. As a result, these computer-assisted methods have difficulties in extracting noncoherent dislocated horizons. We have developed a new data-driven method to correlate, track, and extract horizons from seismic volumes with complex geologic structures. Our method correlates seismic horizons across discontinuities and does not require user input in the form of seed points or prior identification of faults. Furthermore, the method is robust toward amplitude changes along a seismic horizon and does not jump from peak to trough or vice versa. We use a large sliding window and match full-length seismic traces using nonlocal dynamic time warping to extract grids of correlated points for our target horizons. Through computed accuracy measurements, we discard nonaccurate correlations before interpolating complete seismic horizons. Because our method does not require manually picked seed points or prior structural restoration, it does not rely on interpretive experience or geologic knowledge. The proposed method is applied on different real and complex seismic images, with two case examples from the southwestern Barents Sea, and one on the open source Netherlands F3 seismic data.

INTRODUCTION

Tracking dislocated and truncated horizons in seismic images presents difficulties for manual and automatic interpretation. Figure 1 illustrates a manually interpreted complex seismic image of the Polhem Subplatform in the southwestern Barents Sea. Whereas the horizons of the Pleistocene and Paleocene sequences (green and yellow) are relatively coherent laterally, the rotated and eroded fault blocks of the Mesozoic sequence (blue) are challenging to interpret because the seismic horizons are vertically and laterally dislocated as well as truncated by an unconformity.

The state-of-the-art seismic interpretation workflow offered in numerous software packages involves manually picking seed points along seismic horizons in seismic images and interpolating between these seed points using coherency-based autotracking tools. Although autotracking tools simplify the interpretation process, picking seed points and manually quality-checking miscorrelations require significant interpretive experience and geologic knowledge. One reason for this is that the autotracking may not stop tracking a horizon at major faults, forcing the user to generate new seed points within adjacent fault blocks corresponding to the same stratigraphic unit (as illustrated in Figure 1). Unconformities caused by significant erosion are particularly challenging to address because they tend to truncate seismic horizons.

In the past few decades, different computational and computer-assisted horizon extraction methods have been introduced as alternatives to the process of manually picking seed points, aiming to further automate the seismic interpretive workflow, process multidimensional data concurrently, and reduce the need for user interaction. Some of the more interesting horizon-extraction methods are based on local reflection slopes (e.g., Bakker, 2002; Lomask et al., 2006), unwrapped instantaneous phase (e.g., Stark, 2003, 2005; Wu and Zhong, 2012), and dynamic time warping (DTW) (e.g., Hale, 2013; Wu and Hale, 2016a; Wu and Fomel, 2018)

Local reflection slope methods involve using structure tensors and an iterative least-squares fitting of horizon slopes with local reflections slopes (Bakker, 2002; Lomask et al., 2006). In general, horizon tracking using local reflection slopes effectively tracks coherent seismic horizons but is sensitive to faults and other discontinuities.

Additionally, local reflection slope methods often cause a tracked horizon to jump from peak to trough or vice versa, due to the lack of amplitude or phase information (Bakker, 2002).

Instantaneous phase is commonly used to complement seismic amplitude information for seismic interpretation (Taner et al., 1979), and methods using unwrapped instantaneous phase for horizon extraction have been proposed by, e.g., Stark (2003, 2005) and Wu and Zhong (2012). Stark (2003) generate relative geologic time (RGT) cubes from unwrapped phase volumes, and then extract seismic horizons directly from the RGT cubes. This method is based on the assumptions that continuous seismic horizons follow constant instantaneous phase values, and that the unwrapped phase represents RGT in a given seismic volume or image (Stark, 2003, 2005). Wu and Zhong (2012) propose an extension to Stark's method by implementing horizon and unconformity constraints into a 3D unwrapping process. They show that the implementation of these constraints significantly improves the reliability of the RGT volume, assuming that the user has unconformities and reliable horizons or segments of reliable horizons prior to the unwrapping operation.

DTW was originally introduced as a pattern-matching algorithm for speech recognition in 1978 by Sakoe and Chiba. The algorithm finds the optimal alignment of two time series by nonlinearly stretching and shrinking of one time series along its time axis until it is "warped" into the other. DTW is effective and accurate in matching time series with nonlinear fluctuations along the time axis, as speech patterns and seismic traces typically have. Since the introduction of DTW in 1978, there have been suggested different improvements to the algorithm. Among these suggestions is the use of slope constraints. The commonly used slope constraints are the Sakoe-Chiba band (Sakoe and Chiba, 1978) and the Itakura parallelogram (Itakura,

1975). Slope constraints will control the warping by preventing that short segments of a pattern are matched with full-length pattern segment or vice versa. Generally, the use of slope constraint speeds up the DTW computation but may lead to undesirable trace correlation if the choice of slope constraint and its parameters are not carefully selected.

In geophysics, DTW has proven useful to correlate well-to-well logs (e.g., Anderson and Gaby, 1983; Lineman et al., 1987) and to match seismic traces (e.g., Hale, 2013; Wu and Fomel, 2018). Hale (2013) presents a method for dynamic warping of seismic images to estimate fault throws in seismic images, and to estimate registration (alignment) of PP and PS images. Hale's method is an extension to an approximation of the original DTW algorithm (Mottl et al., 2002), where alignment errors are smoothed nonlinearly along each image dimension before the DTW operation estimate shifts in the seismic image. Wu and Hale (2016a) proposed a full interpretive workflow to automatically extract horizons from flattened seismic images. Their workflow includes (1) fault identification and unfaulting of seismic images, (2) unconformity identification, (3) unconformity-constrained image flattening, and (4) horizon extraction from the flattened seismic image (Wu and Hale, 2015a, 2015b, 2016b). Wu and Hale's (2016a) interpretive workflow addresses many important challenges in seismic interpretation but the steps related to their fault processing and unconformity processing are complicated and may affect the flattening operation, which in turn affects the horizon extraction.

More recently, Wu and Fomel (2018) proposed to extract horizons by fitting, in the least-squares sense, the local slopes and multigrid correlations of seismic traces. In this method, the local slopes, computed from structure tensors (Hale, 2009; Wu and Janson, 2017), are helpful to fit a horizon that smoothly and consistently follows local reflection structures in areas without structural discontinuities. The multigrid correlations, calculated by using DTW, are helpful to track a horizon that is dislocated by faults and to follow consistent phases (e.g., zeros, peaks, or troughs).

In this paper, we present a completely data-driven 3D method to automatically correlate, track, and extract seismic horizons from complex seismic volumes. For this, we use nonlocal DTW and unwrapped instantaneous phase. The method that we present does not rely on manually selected seed points, and it is insensitive to amplitude changes along a reflector. Furthermore, it is robust to faulting without the requirement of prior fault identification or image flattening. With different case examples, we test the proposed interpretive method and extract seismic horizons from real 3D seismic images containing complex structures such as heavily faulted successions and rotated fault blocks.

METHOD

We present a fully data-driven method on horizon extraction from complex seismic images. First, we use DTW to match nonlocal seismic traces within a large sliding 3D window and correlate horizon grids for any target horizon. Next, to interpolate these horizon grids we use linear interpolation and implement an unwrapped instantaneous phase-constraint.

Dynamic time warping

We use the original DTW algorithm as described by Sakoe and Chiba (1978) to match seismic traces and extract seismic horizons.
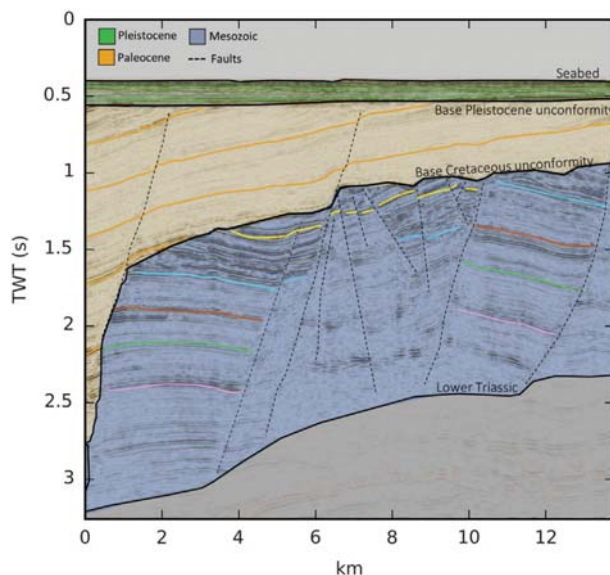

Figure 1. A manually interpreted seismic image of the Polhem Subplatform in the southwestern Barents Sea. The Polhem Subplatform is structurally and stratigraphically complex, with stratigraphic sequences that are separated by unconformities and rotated fault blocks offset by major faults. The main stratigraphic sequences are annotated with colors: green (Pleistocene), orange (Paleocene), and blue (Mesozoic). Major faults are annotated with stippled black lines, and target horizons and unconformities are annotated with complete colored and black lines.

Sakoe and Chiba (1978) define a warp function F between two time series X and Y (sampled with the same sample rate) as

$$F = C_1, C_2, \ldots, C_k, \ldots, C_K, \qquad (1)$$

where C is a point $C_k(i, j)$, K is the length of the warp path, and the time series can be written as

$$\text{trace X} = x_1, x_2, \ldots, x_i, \ldots, x_I, \quad \text{and}$$
$$\text{trace Y} = y_1, y_2, \ldots, y_j, \ldots, y_J. \qquad (2)$$

Then, the optimal warp function is obtained by finding the minimum distance warp path that describes the relationship of all the samples along the two time series:

$$\text{Dist}(F) = \sum_{k=1}^{k=K} \text{Dist}(C_{ki}, C_{kj}). \qquad (3)$$

The minimum distance warp path provides a pair-wise matching of all trace indexes, meaning that every time sample along trace X is optimally matched with at least one time sample along trace Y and $\text{Dist}(C_{ki}, C_{kj})$ is the distance between a time sample in trace X and the correlated time sample in trace Y. The warp path is a 2D matrix in which each row represents a pair of matched time samples along trace X and trace Y. Figure 2 shows the optimal alignment of two seismic traces with DTW, as well as their warp path. We use this warp path to track and extract reflective events, assumed to represent seismic horizons. Because DTW is a pattern matching operation, it does not mainly rely on amplitude values. This is an advantage as seismic amplitudes can vary a lot along the same seismic horizon.

Although several suggestions to optimize DTW include the use of slope constraint (Itakura, 1975; Sakoe and Chiba, 1978), we do not implement this here. Conventional slope constraints as the Sakoe-Chiba band and the Itakura parallelogram set the limit on how much the warp path can differ from a diagonal line with fixed bands, and implementing such slope constraints in this study would require known true geologic dip and known fault throws. Because optimal

implementation of slope constraints for DTW of seismic traces in structurally complex geologic settings is particularly challenging, we use the original DTW algorithm without slope constraints. Instead, we deal with potential nonaccurate correlations (outliers) by measuring correlation consistency and implement an accuracy criterion. To correlate seismic traces, we perform nonlocal trace matching with DTW for every trace-pair within a defined window to get their warp path. Then, we extract any number of seismic horizons from the matched time samples stored in the warp paths. Figure 3 illustrates how two matched reflective events (red and blue) represent the same seismic horizon, and how we use DTW to track seismic horizons. The pseudocode in Table 1 shows how we apply nonlocal DTW within a given window.

To extract horizons from 3D seismic images, we set up a grid of seismic traces, e.g., every 5th, 10th, or 20th inline and crossline location, and then we use a large sliding window to iteratively match every pair of the gridded traces within the window. The grid step and the window size are the key parameters for this operation, and it is crucial to ensure enough traces represented on each side of a discontinuity for optimal correlation of displaced horizons. By increasing the grid step, we increase computational efficiency. Figure 4 illustrates the importance of a large window size for a seismic scale fault. The lateral size of the window has to be larger than the horizontal fault displacement to properly correlate a dislocated horizon across a fault. In the example illustrated in Figure 4, a successful correlation requires a window size of at least 0.75×0.75 km (30×30 traces). For larger and more structurally complex seismic volumes, as we show with case examples in the next section, larger window sizes are necessary.

The DTW operation matches all time samples, and it is possible to extract a seismic horizon for any given time sample along a selected trace. However, we extract only horizons that follow distinct peaks and troughs, selected automatically with a peak detection algorithm (illustrated in Figure 2). The peak detection identifies the most significant peaks and troughs along an arbitrary trace, where each selected peak and trough can be thought of as a seed point for one horizon. Therefore, the number of selected peaks and troughs along the arbitrary trace defines the starting point and decides which
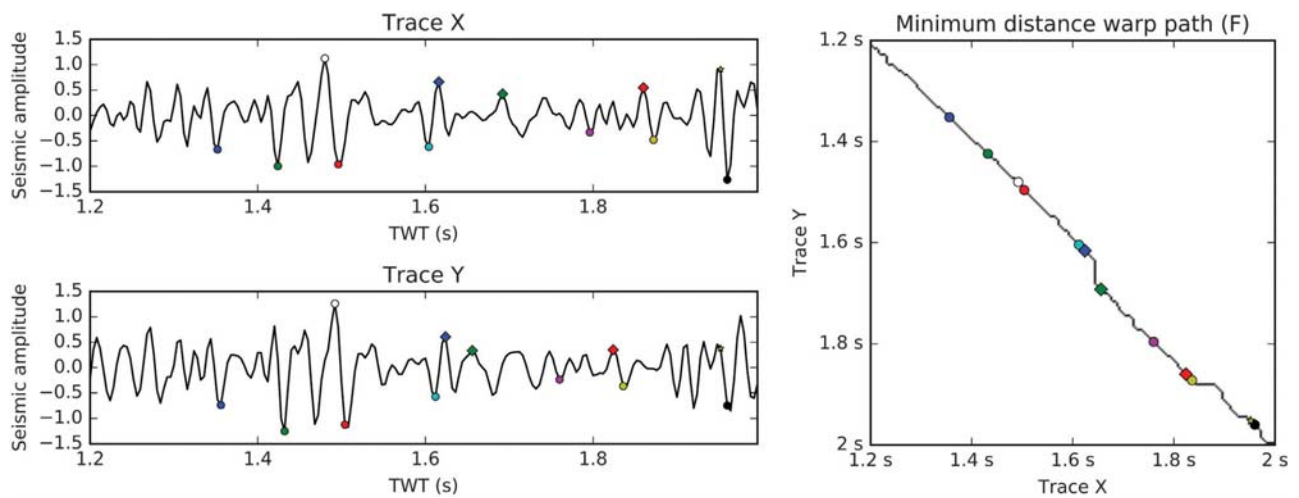

Figure 2. Selected peaks and troughs indicated with colored markers along two traces, X and Y, show their optimal alignment using DTW. DTW provides a minimum distance warp path that describes the relationship of all of the time samples along the two traces.

and how many seismic horizons we extract. By tracking matched points from the stored warp paths, we obtain correlated grids of points where each correlated grid represents a target horizon (Figure 3).

Because we use a sliding window and iteratively match traces, each trace will be revisited multiple times, and this iterative process may produce several possible locations for a reflective event in the correlated grids. We exploit this iterative process to record an

uncertainty measure for each point along a tracked horizon, keep the most accurate correlations, and discard nonaccurate correlations. The accuracy measurement is a calculated relationship between how many times a trace is revisited and how many of these revisitations provide the same location for a point along a target horizon. Figure 5 displays a correlated grid for a target horizon extracted from a small seismic section, before and after removal of nonaccurate correlations. The color bar in Figure 5a–5b indicates
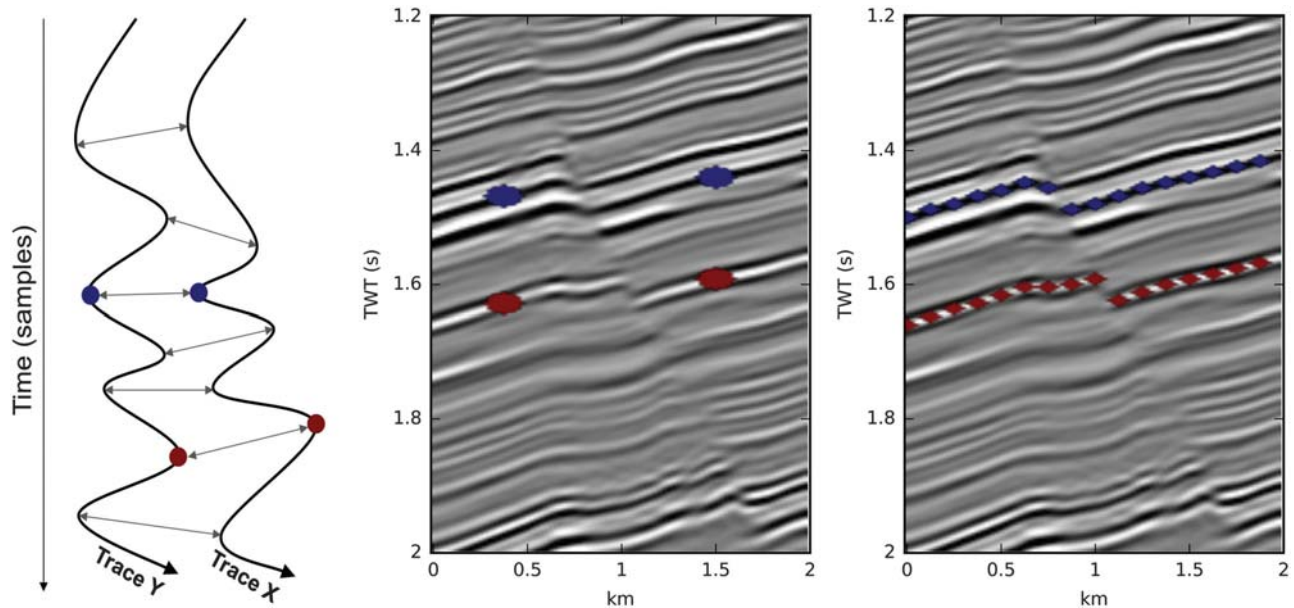
Figure 3. The figure illustrates two reflective events, annotated with red and blue dots, superimposed onto a small faulted seismic image. The reflective events are extracted (left) from the warp path of two seismic traces, X and Y, and then (right) from the warp paths of multiple seismic traces.

Table 1. Simplified Python pseudocode for DTW of gridded seismic traces in a given window.

```
# non-local DTW of gridded seismic traces within a given window
#Define a grid of seismic traces and a window size for the sliding window
#Do DTW for every pair of traces within the window
#Move the sliding window one grid step and repeat DTW operation for all window locations in the seismic
volume
from tslearn import DynamicTimeWarping
grid_step=10
window_size=100
Window = seismic_volume[xl:grid_step:xl+window_size, il:grid_step:il+window_size
warp_paths=[]
for each trace, i, in window:
  traceX= window[i]
  for each trace, j, in window:
    traceY= window[j]
    path= DynamicTimeWarping (traceX, traceY)
  warp_paths.append([traceX, traceY, path])
```

correlation accuracy, and we observe that all the high accurate correlations lie along the same seismic horizon, whereas low-accurate points typically are more scattered. Additionally, we observe that there is typically one point with significantly higher accuracy than the other at each grid location, which makes it easy to set the parameter for the filter operation. Figure 5b and 5c shows the correlated grid after the removal of correlations with less than 30% accuracy.

Unwrapped instantaneous phase

With nonlocal DTW, we can correlate and extract horizon grids for any target horizon. To obtain complete seismic horizons, we interpolate these correlated grids (illustrated in Figure 5). With many different ways to do the interpolation, we have chosen a linear interpolation for 3D grids, where the x-, y-, and z-coordinates represent the inline location, crossline location, and time sample for a given point in one horizon grid. This way, the interpolation is amplitude-independent. To ensure that we do not interpolate across faults or discontinuities or include potential outliers; we implement an unwrapped instantaneous phase constraint for neighboring points.

The instantaneous phase shows the continuity of weak and strong coherent amplitude reflections, and it is a wrapped phase, meaning that the phase at a given time sample along a trace is constrained to the range $-\pi$ to π of the phase offset. Unwrapping these phase values will provide a continuous time function, where the unwrapped phase values should generally increase with the increasing traveltime (Herraez et al., 2002; Abdul-Rahman et al., 2005). A large number of phase wrapping operators exist today, and there is no standard phase wrapping operator or one standard way of solving the phase unwrapping problem. Mathematically, phase wrapping is expressed as

$$x_w(n) = W[x(n)], \qquad (4)$$

where $x(n)$ is the continuous phase signal, W is the phase-wrapping operator, and $x_w(n)$ is the wrapped signal.

As proposed by Stark (2003, 2005), the unwrapped instantaneous phase can be used to generate an RGT where the unwrapped phase value represents an RGT in a given seismic volume. However, the phase unwrapping of seismic instantaneous phase volumes will suffer in the
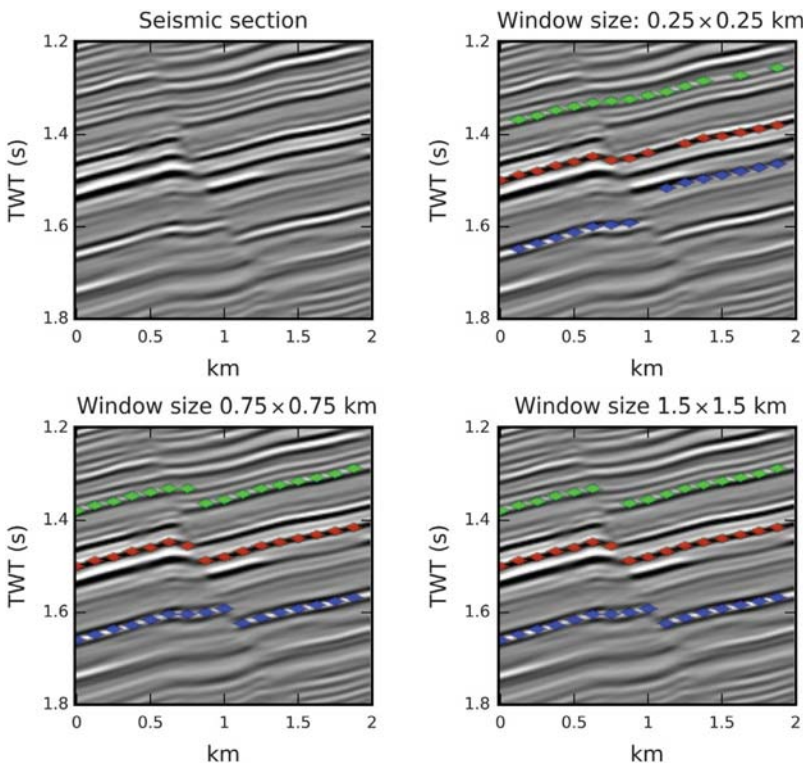

Figure 4. Nonlocal DTW requires a large window size to successfully handle dislocated seismic horizons. The figure illustrates the tracking of three target horizons with window sizes of 0.25×0.25, 0.75×0.75, and 1.5×1.5 km, all with a grid step of 0.125 km. This shows that optimal correlation is only obtained for window size of 0.75×0.75 km $(30 \times 30$ traces) or larger.
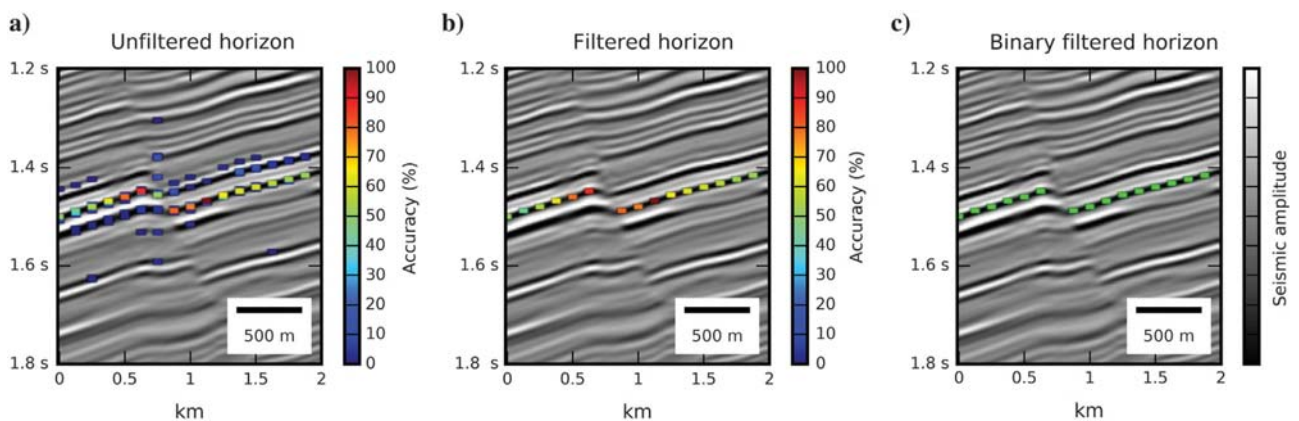

Figure 5. A sliding DTW window allows us to record an accuracy measurement while correlating seismic horizons. This figure shows (a) an unfiltered horizon grid, (b) the target horizon after accuracy filtering with a 30% accuracy criterion, and (c) a binary representation of the filtered horizon. The color bars in (a) and (b) indicate the correlation consistency in percent per grid location.

presence of faults and discontinuities, particularly unconformities. Wu and Zhong's (2012) suggestion to implement horizon and unconformity constraints to the unwrapping operation will improve the reliability of the RGT volume. This implementation requires, of course, manual or automated interpretation of unconformities and horizon or horizon segments, which are not trivial prerequisites. Our approach differs in that we only use unwrapped phase to constrain interpolation between already correlated neighboring points. We use a 3D phase unwrapping algorithm based on sorting by reliability (3D-SRA) following a noncontinuous path, proposed by Abdul-Rahman et al. (2005).

We interpolate between neighboring correlated points using a linear interpolation approach (curve fitting) and use an interpolation constraint that only allows interpolation when the unwrapped phase values are continuous. Points in a horizon grid with no neighbors allowed for interpolation will be discarded. This will result in inter-
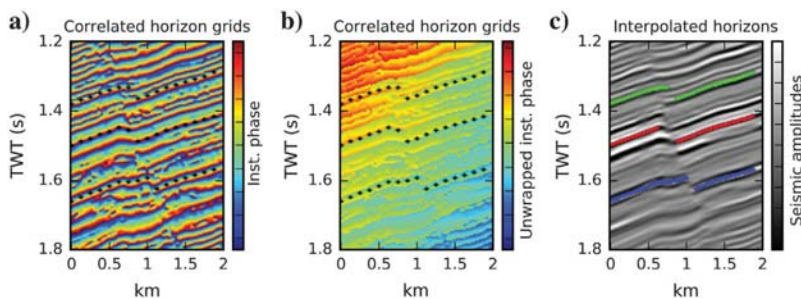

Figure 6. The figure shows correlated horizon grids for three target horizons superimposed onto (a) instantaneous phase and (b) unwrapped instantaneous phase, and (c) the original seismic image with superimposed interpolated seismic horizons. With an unwrapped instantaneous phase constraint, we ensure an optimal interpolation of horizon grids that respect faults and are robust to potential outliers.
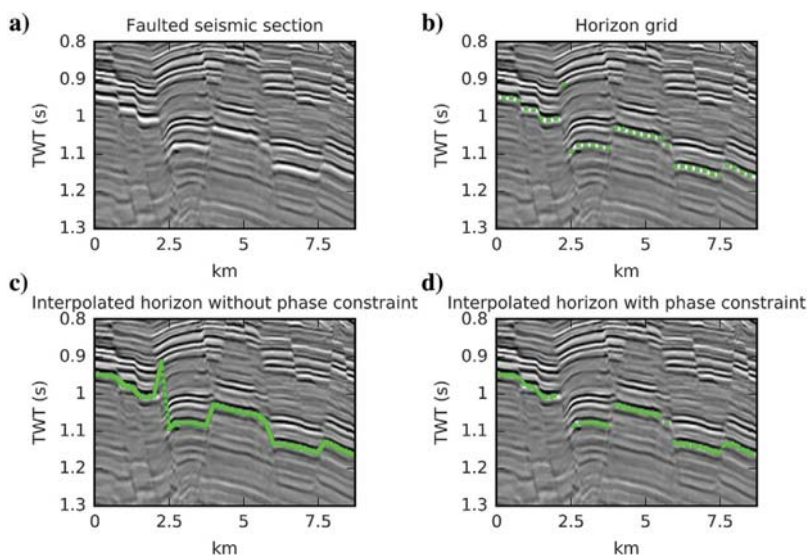

Figure 7. The figure shows a crossline from faulted seismic section of size 350 inlines × 400 crosslines with a bin size of 25 m. The correlated grid of a target horizon (b) verifies that the DTW operation is robust to faults. Linear interpolation of the correlated grid will cut across faults and include outliers, which show as spikes (c), whereas interpolation with our implemented phase constraint will respect faults and disregard outliers (d).

polation along coherent segments of the horizons, where the reflective event consistently follows a peak or trough, with no interpolation across faults or other disruptions in the seismic image (Figure 6). The implementation of this constraint will therefore discard potential outliers in the original correlated grid, as illustrated in Figure 7. In Figure 7, we show a faulted seismic section, with the correlated grid for a target horizon and interpolation of this grid with and without the implementation of phase constraint. Without the implemented phase constraint, the interpolated seismic horizon cuts across faults and fault zones and includes outliers that appear as "spikes."

RESULTS AND DISCUSSION

We test the proposed method for horizon extraction in different complex geologic settings. For comparability and reproducibility, we include a case study example from a publicly available seismic volume (Netherlands F3). We also include two case examples from the Barents Sea, one on a heavily faulted section with large normal faults from the Loppa High and one on eroded and rotated Mesozoic fault blocks on the adjacent Polhem Subplatform. Figure 8 shows the map of the southwestern Barents Sea with structural elements on the Base Cretaceous Unconformity and with the location of the Loppa High and the Polhem Subplatform.

Offshore Netherlands F3

Figure 9 shows a subset of the publicly available Netherlands F3 dataset, acquired in the North Sea, offshore Netherlands. The subset includes 262 samples × 300 crosslines × 951 inlines acquired with a sample rate of 4 ms and a bin size of 25 m. The Netherlands F3 data set covers a large deltaic system with deposits from the Late Jurassic to Early Cretaceous (Sørensen et al., 1997). The subset is structurally complex with salt present near the bottom of the volume, folds, and a few large-offset faults. With our proposed method, we extract correlated grids of points for six target horizons. Using a 2.5×2.5 km (100×100 traces) sized window and a grid step of 0.5 km, the DTW operation takes 68.6 min with an Intel Core i7-6500U CPU processor for the seismic subset. To obtain a denser grid, we reapply a small fixed DTW window around each correlated point, this time with a 0.5×0.5 km window size and a grid step of 0.125 km. The second operation takes an additional 56.8 min, whereas the time it takes to extract one horizon grid is less than a minute.

Figure 9 shows sparse and dense correlated horizon grids before the phase-constrained interpolation; therefore, occasional miscorrelations occur. We observe that the more distinct seismic horizons (such as the two darker blue, the orange, and the red) result in more consistent tracking. Figure 10 presents a time map and an amplitude map (the top views) of the orange horizon in
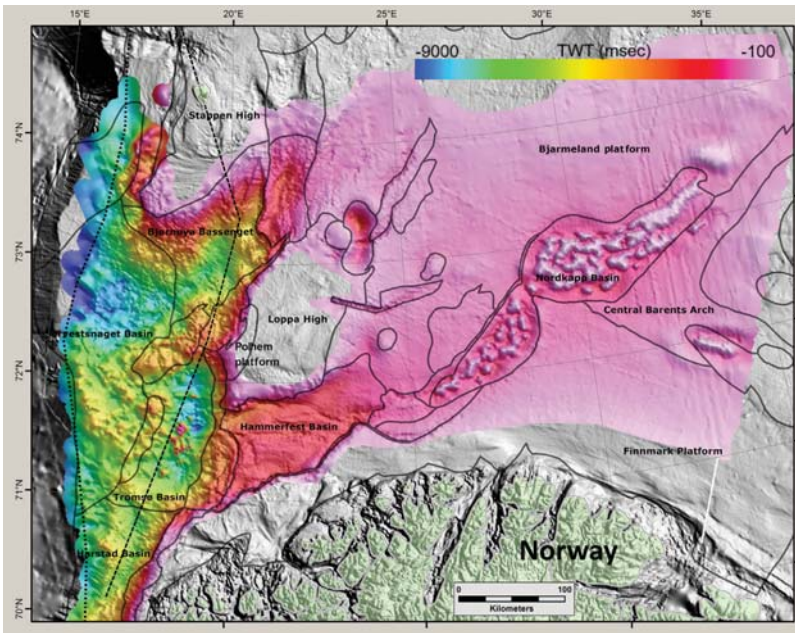
Figure 8. Regional map of the southwestern Barents Sea, north of Norway, where the color bar indicates the depth of the Base Cretaceous Unconformity in two-way traveltime (TWT). The map shows annotated structural elements, such as the Loppa High and the Polhem Subplatform, which are locations for two of our case examples.
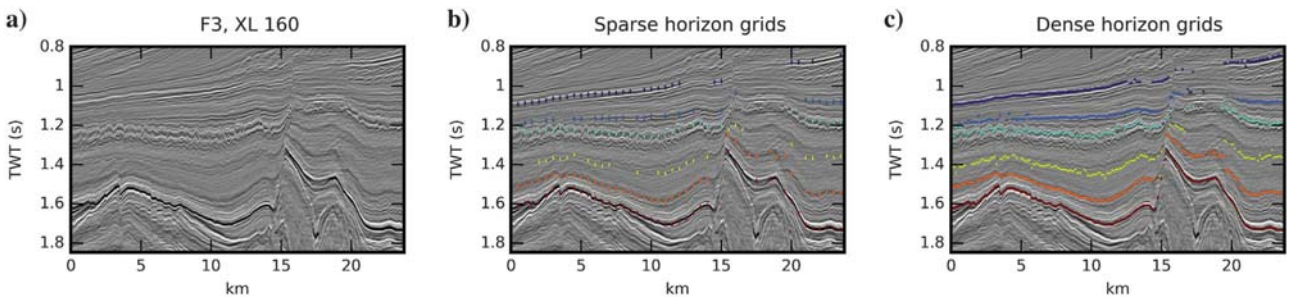

Figure 9. A subset of the F3 Netherlands seismic volume (a) with salt present near the bottom of the subset. Nonlocal DTW provides correlated horizon grids (prior to interpolation) for six target horizons indicated with the colors dark blue, blue, cyan, yellow, orange, and red. The figure illustrates correlated horizons with a (b) sparse and (c) dense grid.
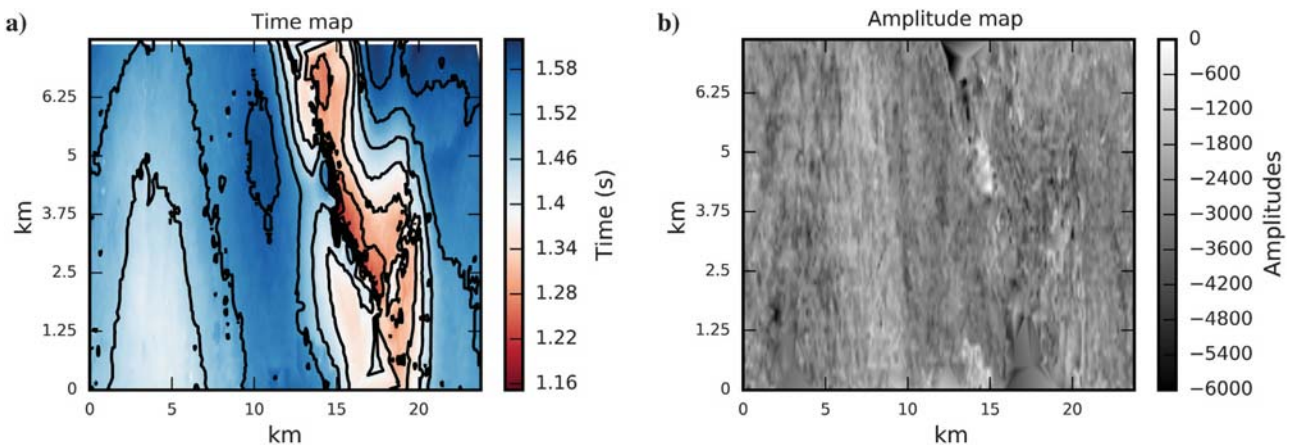
Figure 10. (a) Time map and (b) amplitude map for a correlated target horizon (the orange horizon in Figure 9). The colors in the contoured time map can be assumed to", this is unnecessary illustrate differences in depth, where the shallow areas (red and white) indicate the lateral extent of the salt dome. The amplitude map shows that the horizon is consistently tracked along a trough, with no jumping from trough to peak and with seismic amplitudes mostly ranging from −4000 to −2000.

Figure 9. The time map indicates the lateral extent of the salt dome with shallow areas (in red and white). The amplitude map shows that there is no jumping from peak to trough along the extracted horizon.

Heavily faulted Triassic strata, southwestern Barents Sea

With this case example, we show horizon extraction from a small structurally complex seismic volume, covering Triassic successions with major Jurassic normal faults from the Loppa High in the southwestern Barents Sea, north of Norway (Figure 8). The southwestern Barents Sea sedimentary packages range in age from Late Paleozoic to the present (Faleide et al., 1993; Breivik et al.,

1998; Glørstad-Clark et al., 2010), and it has experienced a complex history of crustal thinning with several rift phases contributing to a series of rifting, subsidence, tilting, uplift, erosion, and inversion events. These rift phases have led to the formation of the basins and highs in the Barents Sea, such as the Loppa High (Gabrielsen et al., 1990, 1993; Faleide et al., 1993; Gudlaugsson et al., 1998; Glørstad-Clark et al., 2010).

The Loppa High was, prior to its inversion in the Early Cretaceous (Indrevær et al., 2017), a major Mesozoic sedimentary depocenter with a strong sedimentary influx and an accumulation of prograding deltaic wedges providing thick, mainly Triassic, successions in the area (Glørstad-Clark et al., 2010, 2011). The subsequent tectonic activity caused the Mesozoic strata to experience massive normal faulting and fault block rotation in the Jurassic (Gabrielsen et al., 1990, 1993; Faleide et al., 1993).

The seismic data used in this case example are post stack time migrated (PSTM) TopSeis data from the first-ever marine source-over-cable acquisition (Lie et al., 2018) with a bandwidth of 4–110 Hz. The data cover 1000 inlines and 400 crosslines from 0.7 to 1.6 s, with a bin size of 25 m and a sample rate of 4 ms. We use a window size of 2.5×2.5 km and a grid step of 0.5 km. Figure 11 shows the correlated grid for one target horizon before interpolation where colors indicate the correlation accuracy for each point (Figure 11a and 11b), and the complete horizon after phase-constrained interpolation (Figure 11c and 11d). The dislocated horizon is optimally correlated across faults. By flattening the seismic section on our target horizon, we verify the data-driven horizon tracking (Figure 12).
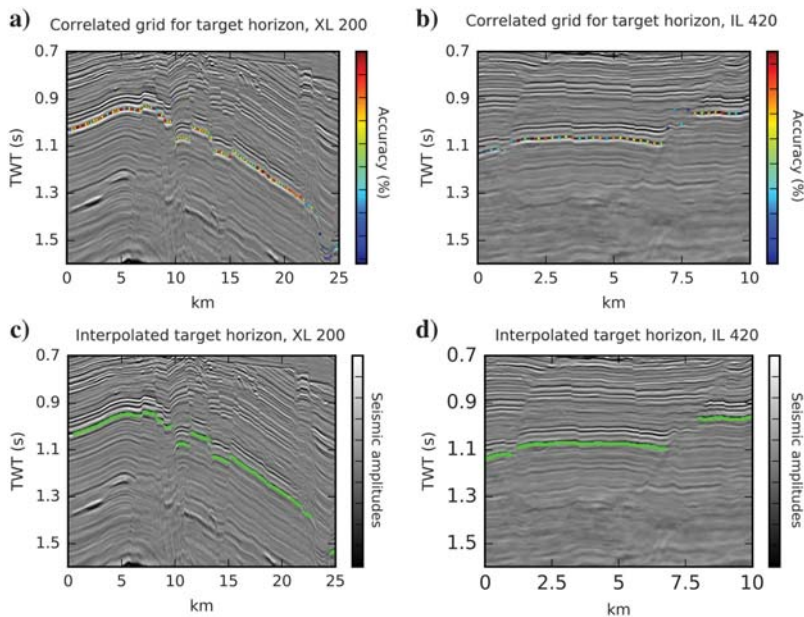

Figure 11. The figure shows inline and crossline views for one correlated target horizon in a heavily faulted seismic image from the southwestern Barents Sea before (a and b) and after (c and d) interpolation. The color bars in a and b illustrate correlation accuracy.

Rotated and eroded fault blocks, southwestern Barents Sea

With this case example, we specifically target Mesozoic fault blocks on the Polhem Subplatform (Figures 1 and 8), situated on the western margin of the Loppa High in the southwestern Barents Sea (Gabrielsen et al., 1990). The seismic data used in this case example are conventional 8–80 Hz PSTM data that cover 551 inlines and 351 crosslines laterally with a bin size of 25 m and 3.5 s in time with a sample rate of 4 ms. The targeted fault blocks are truncated by the Base Cretaceous Unconformity separating them from the overlying Paleocene strata that prograded westward into the Tromsø Basin (Faleide et al., 1993; Glørstad-Clark et al., 2010). Figure 1 shows a seismic image from the Polhem Subplatform with annotations of the main stratigraphic successions, unconformities, and major Jurassic faults.

Unconformities are erosional events or nondepositional hiatuses that leave geologic time gaps in seismic images. Erosional surfaces that truncate seismic reflections are particularly challenging to address and will complicate horizon tracking. By implementing unconformity constraints, we can track and extract seismic horizons from defined stratigraphic sequences (Wu and Hale, 2015b). The data-driven methods for unconformity identification and extraction are typically not straightforward to implement in an interpretation workflow, but they do exist (e.g., Barnes, 2000; Hoek et al., 2010;
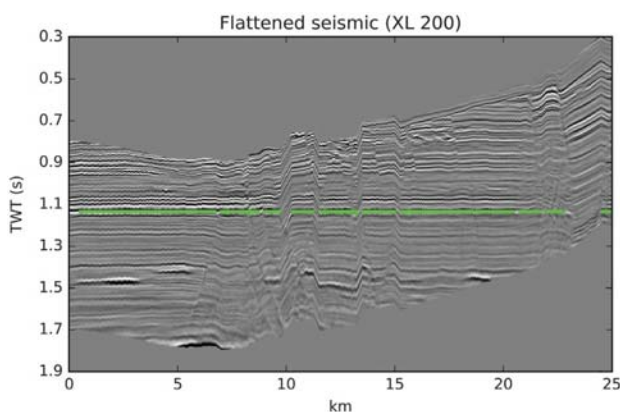

Figure 12. To evaluate the extracted target horizon showed in Figure 11, we flatten the seismic image on the target horizon. The flattened seismic image indicates successful extraction of the target horizon.
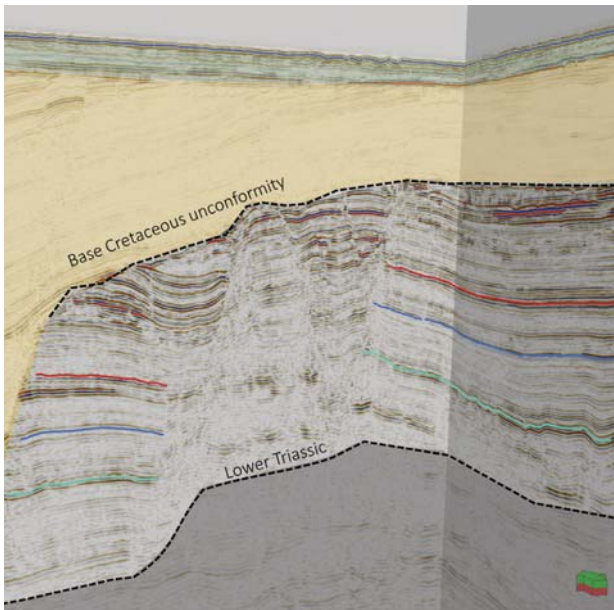
Figure 13. A 3D view of an intersecting inline and crossline, with three seismic horizons extracted from a seismic section constrained by unconformities. The unconformities have been identified with a semiautomatic method (Bugge et al., 2018), and the seismic horizons are correlated with the method proposed in this study. The case example covers part of the Polhem Subplatform in the southwestern Barents Sea, as illustrated in Figure 1, which includes annotated stratigraphic and structural details.

Wu and Hale, 2013, 2015a; Qayyum et al., 2017, 2018; Bugge et al., 2018). Here, we use a semiautomated method for unconformity extraction introduced by Bugge et al. (2018) to constrain our target sequence. This method assumes that the stratigraphic stacking pattern and the seismic amplitudes above and below an unconformity are significantly different.

With known unconformities, we constrain the Mesozoic succession on the Polhem Subplatform and we correlate dislocated seismic horizons within the fault blocks. Figure 13 shows a 3D view of the three extracted seismic horizons within the constrained Mesozoic succession. Ongoing work for further improvements to a fully automatic seismic interpretive workflow includes data-driven identification of stratigraphic sequences to automatically define unconformity constraints. This is, however, beyond the scope of this paper.

CONCLUSION

We present a new 3D method on data-driven horizon extraction from seismic images with nonlocal DTW and unwrapped instantaneous phase, and we apply the method on real and complex case examples. With a large sliding window, we match full-length seismic traces to extract a correlated grid of points for any target horizon in a seismic cube. Through computed accuracy measurements, we discard non-accurate correlations and implement an unwrapped phase constraint before we interpolate the grids and extract complete seismic horizons.

The proposed horizon extraction method is insensitive toward amplitude changes along a seismic horizon without jumping between peaks and troughs. We show this with the Netherlands F3

case example. Furthermore, the method is robust to faulting without prior identification of faults, as shown in the case example on the heavily faulted Triassic section from the southwestern Barents Sea. Stratigraphically complex seismic images, where seismic horizons are truncated by erosional surfaces, require unconformity-constrained horizon extraction. With the case example from the Polhem Subplatform in the southwestern Barents Sea, we show how to implement unconformity constraints and correlate seismic horizons across rotated and eroded fault blocks. Because we extract dislocated seismic horizon without any manually selected seed points or any prior structural restoration, we do not rely on interpretive experience or geologic knowledge.

DATA AND MATERIALS AVAILABILITY

The seismic data associated with this research are confidential and cannot be released. Python source code and tutorial is available through https://github.com/ajbugge/HorizonTracker.

REFERENCES

Abdul-Rahman, H., M. Gdeisat, D. Burton, and M. Lalor, 2005, Fast three-dimensional phase-unwrapping algorithm based on sorting by reliability following a non-continuous path: Optical Measurement Systems for Industrial Inspection IV, 5856, 32–40, doi: 10.1117/12.611415.

Anderson, K. R., and J. E. Gaby, 1983, Dynamic waveform matching: Information Sciences, 31, 221–242, doi: 10.1016/0020-0255(83)90054-3.

Bakker, P., 2002, Image structure analysis for seismic interpretation: Ph.D. thesis, Delft University of Technology.

Barnes, A. E., 2000, Attributes for automating seismic facies analysis: 70th Annual International Meeting, SEG, Expanded Abstracts, 553–556, doi: 10.1190/1.1816121.

Breivik, A. J., J. I. Faleide, and S. T. Gudlaugson, 1998, Southwestern Barents Sea margin: Late Mesozoic sedimentary basins and crustal extension: Tectonophysics, 293, 21–44, doi: 10.1016/S0040-1951(98)00073-0.

Bugge, A. J., S. R. Clark, J. E. Lie, and J. I. Faleide, 2018, A case study on semiautomatic seismic interpretation of unconformities and faults in the southwestern Barents Sea: Interpretation, 6, no. 2, SD29–SD40, doi: 10.1190/INT-2017-0152.1.

Faleide, J. I., E. Vagnes, and S. T. Gudlaugson, 1993, Late Mesozoic-Cenozoic evolution of the South-Western Barents Sea in a regional rift-shear tectonic setting: Marine and Petroleum Geology, 10, 186–214, doi: 10.1016/0264-8172(93)90104-Z.

Gabrielsen, R. H., R. Færseth, L. N. Jensen, J. E. Kalheim, and F. Riis, 1990, Structural elements of the NCS — Part 1: The Barents Sea region: NPD-Bulletin, 6, 1–47.

Gabrielsen, R. H., I. Grunnaleite, and S. Ottesen, 1993, Reactivation of fault complexes in the Loppa High area, Southwestern Barents Sea: Norwegian Petroleum Society Special Publications, 2, 631–641, doi: 10.1016/B978-0-444-88943-0.50041-1.

Glørstad-Clark, E., E. P. Birkeland, J. P. Nystuen, J. I. Faleide, and I. Midtkandal, 2011, Triassic platform-margin deltas in the western Barents Sea: Marine and Petroleum Geology, 28, 1294–1314, doi: 10.1016/j.marpetgeo.2011.03.006.

Glørstad-Clark, E., J. I. Faleide, B. A. Lundschien, and J. P. Nystuen, 2010, Triassic seismic sequence stratigraphy and paleogeography of the Western Barents Sea area: Marine and Petroleum Geology, 27, 1448–1475, doi: 10.1016/j.marpetgeo.2010.02.008.

Gudlaugsson, S. T., J. I. Faleide, S. E. Johansen, and A. J. Breivik, 1998, Late Palaeozoic structural development of the South-western Barents Sea: Marine and Petroleum Geology, **15**, 73–102, doi: 10.1016/S0264-8172(97)00048-2.

Hale, D., 2009, Image-guided blended neighbor interpolation of scattered data: 79th Annual International Meeting, SEG, Expanded Abstracts, 1127–1131, doi: 10.1190/1.3255050.

Hale, D., 2013, Dynamic warping of seismic images: Geophysics, **78**, no. 2, S105–S115, doi: 10.1190/geo2012-0327.1.

Herraez, M. A., D. R. Burton, M. J. Lalor, and M. A. Gdeisat, 2002, Fast two-dimensional phase-unwrapping algorithm based on sorting by reliability following a noncontinuous path: Applied Optics, **41**, 7437–7444, doi: 10.1364/AO.41.007437.

Hoek, T., T. Gesbert, and J. Pickens, 2010, Geometric attributes for seismic stratigraphic interpretation: The Leading Edge, **29**, 1056–1065, doi: 10.1190/1.3485766.

Indrevær, K., R. H. Gabrielsen, and J. I. Faleide, 2017, Early cretaceous synrift uplift and tectonic inversion in the Loppa High area, southwestern Barents Sea, Norwegian shelf: Journal of the Geological Society, **174**, 242–254, doi: 10.1144/jgs2016-066.

Itakura, F., 1975, Minimum prediction residual principle applied to speech recognition: IEEE Transactions on Acoustics, Speech, and Signal Processing, **23**, 67–72, doi: 10.1109/TASSP.1975.1162641.

Lie, J. E., V. Danielse, P. E. Dhelie, R. Sablon, R. Siliqi, C. Grubb, V. Vinje, and R. Soubaras, 2018, A novel source-over-cable solution to address the Barents Sea imaging challenges: Marine Acquisition Workshop, 1–5.

Lineman, D. J., J. D. Mendelson, and M. N. Toksök, 1987, Well-to-well log correlation using knowledge-based systems and dynamic depth warping: Presented at the SPWLA 28th Annual Logging Symposium.

Lomask, J., A. Guitton, S. Fomel, J. Claerbout, and A. A. Valenciano, 2006, Flattening without picking: Geophysics, **71**, no. 4, P13–P20, doi: 10.1190/1.2210848.

Mottl, V., A. Kopylov, A. Kostin, A. Yermakov, and J. Kittler, 2002, Elastic transformation of the image pixel grid for similarity based face identification: Proceedings of the 16th International Conference on Pattern Recognition, IEEE, 549–552.

Qayyum, F., C. Betzler, and O. Catuneanu, 2017, The wheeler diagram, flattening theory, and time: Marine and Petroleum Geology, **86**, 1417–1430, doi: 10.1016/j.marpetgeo.2017.07.034.

Qayyum, F., C. Betzler, and O. Catuneanu, 2018, Space-time continuum in seismic stratigraphy: Principles and norms: Interpretation, **6**, no. 1, T97–T108, doi: 10.1190/INT-2017-0061.1.

Sakoe, H., and S. Chiba, 1978, Dynamic programming algorithm optimization for spoken word recognition: IEEE Transactions on Acoustics, Speech, and Signal Processing, **26**, 43–49, doi: 10.1109/TASSP.1978.1163055.

Sørensen, J. C., U. Gregersen, M. Breiner, and O. Michelsen, 1997, High frequency sequence stratigraphy of Upper Cenozoic deposits: Marine and Petroleum Geology, **14**, 99–123, doi: 10.1016/S0264-8172(96)00052-9.

Stark, T. J., 2003, Unwrapping instantaneous phase to generate a relative geologic time volume: 73rd Annual International Meeting, SEG, Expanded Abstracts, 1707–1710, doi: 10.1190/1.1844072.

Stark, T. J., 2005, Generation of a 3D seismic "Wheeler diagram" from a high resolution age volume: 75th Annual International Meeting, SEG, Expanded Abstracts, 782–785, doi: 10.1190/1.2148275.

Taner, M. T., F. Koehler, and R. E. Sheriff, 1979, Complex seismic trace analysis: Geophysics, **44**, 1041–1063, doi: 10.1190/1.1440994.

Wu, X., and S. Fomel, 2018, Least-squares horizons with local slopes and multigrid correlations: Geophysics, **83**, no. 4, IM29–IM40, doi: 10.1190/geo2017-0830.1.

Wu, X., and D. Hale, 2013, Extracting horizons and sequence boundaries from 3D seismic images: 83rd Annual International Meeting, SEG, Expanded Abstracts, 1440–1445, doi: 10.1190/segam2013-0296.1.

Wu, X., and D. Hale, 2015a, 3D seismic image processing for unconformities: Geophysics, **80**, no. 2, IM35–IM44, doi: 10.1190/geo2014-0323.1.

Wu, X., and D. Hale, 2015b, Horizon volumes with interpreted constraints: Geophysics, **80**, no. 2, IM21–IM33, doi: 10.1190/geo2014-0212.1.

Wu, X., and D. Hale, 2016a, Automatically interpreting all faults, unconformities, and horizons from 3D seismic images: Interpretation, **4**, no. 2, T227–T237, doi: 10.1190/INT-2015-0160.1.

Wu, X., and D. Hale, 2016b, Moving faults while unfaulting 3D seismic images: Geophysics, **81**, no. 2, IM25–IM33, doi: 10.1190/geo2015-0381.1.

Wu, X., and X. Janson, 2017, Directional structure tensors in estimating seismic structural and stratigraphic orientations: Geophysical Journal International, **210**, 534–548, doi: 10.1093/gji/ggx194.

Wu, X., and G. Zhong, 2012, Generating a relative geologic time volume by 3D graph-cut phase unwrapping method with horizon and unconformity constraints: Geophysics, **77**, no. 4, O21–O34, doi: 10.1190/geo2011-0351.1.